Cell

Cranial Suture Regeneration Mitigates Skull and Neurocognitive Defects in Craniosynostosis

Graphical Abstract

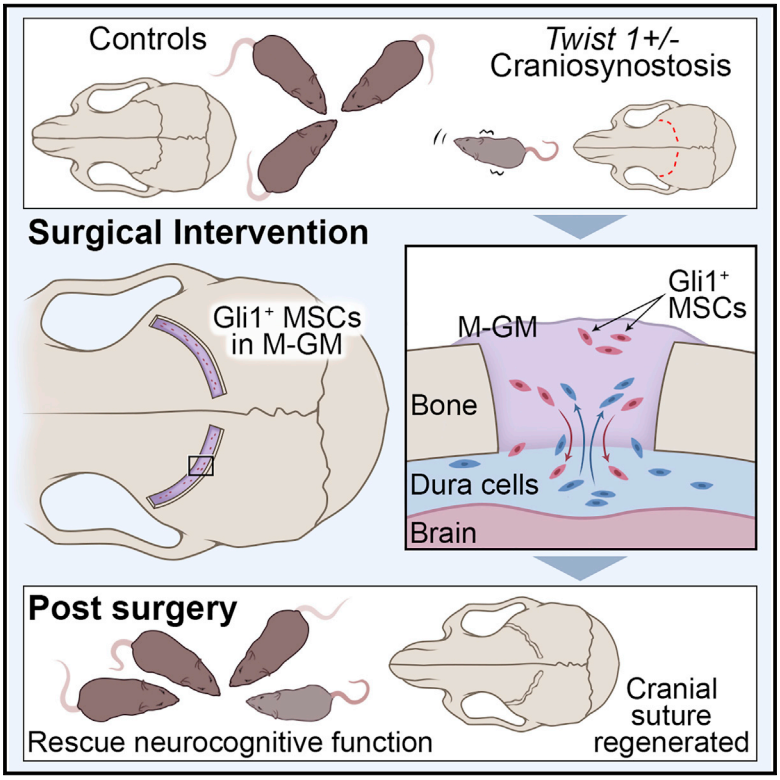

Authors

Mengfei Yu, Li Ma, Yuan Yuan, ..., Berislav V. Zlokovic, Jian-Fu Chen, Yang Chai

Correspondence

ychai@usc.edu

In Brief

Yu et al. develop a platform for cranial suture regeneration using a biodegradable material combined with mesenchymal stem cells in a mouse model of craniosynostosis that reverses increased intracranial pressure and skull and neurocognitive abnormalities.

Highlights

- *Twist1*$^{+/-}$ craniosynostosis mice exhibit elevated ICP and cognitive deficits
- Suture MSCs and resorbable biomaterials can support regeneration of patent suture
- Suture regeneration normalizes *Twist1*$^{+/-}$ ICP, skull shape, and cognitive function
- Suture regeneration offers a biological solution for craniosynostosis patients

Yu et al., 2021, Cell *184*, 243–256
January 7, 2021
https://doi.org/10.1016/j.cell.2020.11.037

CellPress

Cell

CellPress

Article

Cranial Suture Regeneration Mitigates Skull and Neurocognitive Defects in Craniosynostosis

Mengfei Yu,[1,2,5] Li Ma,[1,5] Yuan Yuan,[1,5] Xin Ye,[2] Axel Montagne,[3] Jinzhi He,[1] Thach-Vu Ho,[1] Yingxi Wu,[3] Zhen Zhao,[3] Naomi Sta Maria,[3] Russell Jacobs,[3] Mark Urata,[4] Huiming Wang,[2] Berislav V. Zlokovic,[3] Jian-Fu Chen,[1] and Yang Chai[1,6,*]

[1]Center for Craniofacial Molecular Biology, University of Southern California, 2250 Alcazar Street, CSA 103, Los Angeles, CA 90033, USA

[2]Key Laboratory of Oral Biomedical Research, Affiliated Stomatology Hospital, Zhejiang University School of Medicine, Hangzhou 310003, China

[3]Zilkha Neurogenetic Institute, Keck School of Medicine, University of Southern California, 1501 San Pablo Street, Los Angeles, CA 90033, USA

[4]Division of Plastic and Maxillofacial Surgery, Children's Hospital Los Angeles, Los Angeles, CA 90033, USA

[5]These authors contributed equally

[6]Lead Contact

*Correspondence: ychai@usc.edu

https://doi.org/10.1016/j.cell.2020.11.037

SUMMARY

Craniosynostosis results from premature fusion of the cranial suture(s), which contain mesenchymal stem cells (MSCs) that are crucial for calvarial expansion in coordination with brain growth. Infants with craniosynostosis have skull dysmorphology, increased intracranial pressure, and complications such as neurocognitive impairment that compromise quality of life. Animal models recapitulating these phenotypes are lacking, hampering development of urgently needed innovative therapies. Here, we show that *Twist1*$^{+/-}$ mice with craniosynostosis have increased intracranial pressure and neurocognitive behavioral abnormalities, recapitulating features of human Saethre-Chotzen syndrome. Using a biodegradable material combined with MSCs, we successfully regenerated a functional cranial suture that corrects skull deformity, normalizes intracranial pressure, and rescues neurocognitive behavior deficits. The regenerated suture creates a niche into which endogenous MSCs migrated, sustaining calvarial bone homeostasis and repair. MSC-based cranial suture regeneration offers a paradigm shift in treatment to reverse skull and neurocognitive abnormalities in this devastating disease.

INTRODUCTION

Craniosynostosis is a common disorder in which one or more calvarial sutures, the fibrous joints that separate the skull bones, fuse prematurely in infancy. This causes abnormal skull growth, increased intracranial pressure (ICP), delayed brain development, and often impaired cognitive functions (Morriss-Kay and Wilkie, 2005; Twigg and Wilkie, 2015). Calvarial suture patency is crucial for allowing the skull to compress during childbirth and accommodating its extensive postnatal growth in concert with the developing brain, which continues into adulthood. Currently, the only treatment for craniosynostosis is complex surgery to correct the skull deformity and prevent its sequelae (Wolfswinkel et al., 2017). In many cases, the bones resynostose, necessitating re-operation. There is an immense need for better treatment of craniosynostosis and prevention of resynostosis.

Individuals with craniosynostosis often exhibit neurocognitive dysfunctions and intellectual disabilities (Gripp et al., 2000; Reardon et al., 1997; Speltz et al., 2015; Zechi-Ceide et al., 2012). For example, patients with Saethre-Chotzen syndrome have mutations in *TWIST1* and show preferential loss of the coronal suture. Large deletions including the *TWIST1* locus have been associated with learning disabilities and neurocognitive impairment (Gripp et al., 2000; Zechi-Ceide et al., 2012). Gain-of-function mutations in *ZIC1* or *FGFR* lead to craniosynostosis and learning disabilities (Reardon et al., 1997; Twigg and Wilkie, 2015). Although neurocognitive deficits are more commonly associated with syndromic craniosynostosis, some patients with nonsyndromic single-suture craniosynostosis may develop intellectual disability and developmental delays that vary in severity (Speltz et al., 2015; Wallace et al., 2016; Collett et al., 2017). These studies highlight the heterogeneity of these deficits and provide evidence that craniosynostosis alone may cause neurocognitive dysfunction. Overall, premature suture fusion can adversely affect neurocognition, likely because of increased ICP and neuroanatomical changes (Morriss-Kay and Wilkie, 2005). However, ICP and neurocognition have not been investigated in animal models of craniosynostosis, resulting in a gap in our understanding of this devastating disease. It therefore also remains unknown whether restoring suture patency can improve neurocognitive function.

Mesenchymal stem cells (MSCs) can self-renew and differentiate into an array of different cell types for tissue regeneration

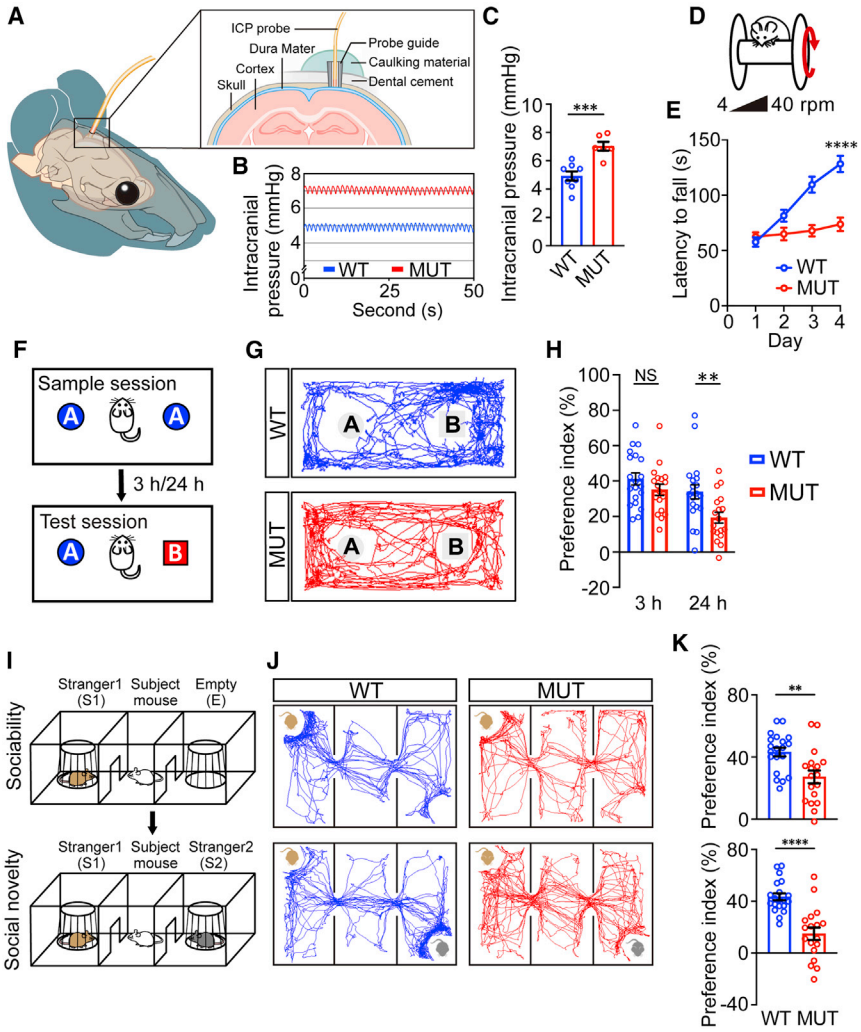

Figure 1. *Twist1*$^{+/-}$ Mice with Craniosynostosis Exhibit Increased ICP and Cognitive Behavioral Abnormalities

(A) Diagram depicting the ICP measurement setup.

(B and C) Representative intracranial pressure (ICP) traces (B) and quantification (C) of ICP values (WT, n = 8; MUT, n = 6 mice).

(D, F, and I) Schematics of the rotarod test (D), novel object test (F), and three-chamber test (I).

(E) Rotarod performance scored as time (seconds) on the rotarod.

(G and J) Representative animal tracks in the novel object test (G) and three-chamber test (J).

(H and K) Preference indices in the novel object test (H) and sociability and social novelty tests (K). WT, wild-type mice, n = 20; MUT, *Twist1*$^{+/-}$ mice with bilateral suture fusion, n = 20.

Data are mean ± SEM (C, E, H, and K). *p < 0.05, **p < 0.01, ***p < 0.001, ****p < 0.0001; NS, not significant; calculated by two-tailed unpaired t test.

(Chan et al., 2018; Mao et al., 2006) and have been used to regenerate calvarial bone (Cowan et al., 2004; Liu et al., 2011; Maruyama et al., 2016). We recently reported that Gli1^{+} cells are an indispensable MSC source within cranial sutures (Zhao et al., 2015). They support craniofacial bone turnover, repair, and regeneration in adult mice (Guo et al., 2018; Park et al., 2016; Zhao et al., 2015). Importantly, we have demonstrated that there is premature loss of Gli1^{+} cells prior to coronal suture fusion in *Twist1*$^{+/-}$ mice (Zhao et al., 2015). These studies suggest that restoring MSCs is a potential therapeutic approach for cranial suture regeneration in craniosynostosis. However, this approach presents substantial technical challenges. Previous studies have shown that the method of MSC delivery and the biomaterial(s) used in the defect area are crucial (Zhao and Chai, 2015). It is not well understood how MSCs may participate in the cranial suture regeneration process or what the ideal biomaterials are to support them.

In this study, we show that premature fusion of the coronal suture led to increased ICP and neurocognitive abnormalities in *Twist1*$^{+/-}$ mice, recapitulating symptoms of Saethre-Chotzen syndrome in humans. Using this clinically highly relevant mouse model, we demonstrated that Gli1^{+} MSCs combined with modified methacrylated gelatin (GelMA) can support coronal suture regeneration. Endogenous MSCs migrated to the regenerated suture area to sustain its function in calvarial tissue homeostasis and repair. Significantly, suture regeneration reduced ICP, partially alleviated calvarial deformity, and improved neurocognitive function. Because TWIST1 haploinsufficiency is associated with craniosynostosis in patients with Saethre-Chotzen syndrome, our discovery is highly relevant for clinical translation and offers a unique approach for improving the quality of life for individuals with craniosynostosis.

RESULTS

Twist1$^{+/-}$ Mice with Craniosynostosis Exhibit Increased ICP and Neurocognitive Abnormalities

To investigate whether craniosynostosis can lead to intracranial hypertension and neurocognitive behavioral abnormalities in *Twist1*$^{+/-}$ mice, as reported in humans (Millichap, 2015), we first measured the ICP in *Twist1*$^{+/-}$ mice with craniosynostosis (referred to as MUT) and wild-type (WT) littermate controls (Figure 1A) at 2 months of age. *Twist1*$^{+/-}$ mice had significantly increased ICP compared with the WT (Figures 1B and 1C). Then we conducted a battery of cognitive behavioral tests. Data from male and female mice were combined for the statistical analyses because no sex-biased preference was observed (Figures S1B–S1G). In open field and elevated plus maze tests, *Twist1*$^{+/-}$ mice spent comparable times in the center area of the open field arena (Figure S1I) and similar times and entries

in the open arms of the elevated plus maze as their WT littermates (Figures S5E–S5G), which indicated that *Twist1*$^{+/-}$ mice did not have unusual levels of anxiety.

In the novel object test (Figure 1F), the preference for a novel object was impaired significantly in *Twist1*$^{+/-}$ mice with craniosynostosis compared with WT controls (Figures 1G and 1H), suggesting a hippocampus-dependent spatial memory deficit. To assess social cognition, a three-chamber test was performed (Figure 1I). The preferences for investigating the mouse versus empty cage and novel versus familiar mouse were decreased significantly in *Twist1*$^{+/-}$ mice with craniosynostosis (Figures 1J and 1K), indicating impaired sociability and social novelty. To exclude the possibility that the impaired cognitive functions in *Twist1*$^{+/-}$ mice with craniosynostosis may be caused by olfactory dysfunction, we performed an odor discrimination/habituation test (Figure S5H) and found that *Twist1*$^{+/-}$ mice with craniosynostosis could distinguish among and habituate to nonsocial and social odors to the same degree as their WT littermates, which suggested that they had normal olfaction (Figure S5I). We examined motor learning ability using a rotarod test (Figure 1D). WT control mice exhibited an increased latency to falling off the accelerating rotarod (4–40 rpm in 5 min) over four consecutive days, indicating active learning (Figure 1E). In contrast, *Twist1*$^{+/-}$ mice with craniosynostosis did not exhibit obvious improvement, suggesting a significant motor learning deficit. We next measured motor functions and did not find an obvious difference in grip strength (Figure S5D) or total distance traveled in the open field arena (Figure S1H), which suggested normal motor strength of *Twist1*$^{+/-}$ mice with suture fusion. These results suggest that *Twist1*$^{+/-}$ mice have neurocognitive dysfunction. We suspected that these deficits were mediated by their elevated ICP because *Twist1* expression is not detected in the brain in adult mice, so its haploinsufficiency is unlikely to have a direct effect on neurocognition (Figure S1A).

Modified GelMA Provides a Favorable Environment for Suture MSCs

To optimize formulation of a scaffold for Gli1^{+} cells to support regeneration of a new coronal suture in *Twist1*$^{+/-}$ mice with craniosynostosis, we compared several different biomaterials. We tested different formulations of GelMA modified with Matrigel and collagen I (COL-I). GelMA has excellent biocompatibility and is easy to use in a surgical setting because it conforms to defects and can be light-cured in seconds (Noshadi et al., 2017). Addition of Matrigel promotes the spread of cells in the scaffold, whereas COL-I helps form a suitable suture space, as shown below. Before settling on the final formulation, we tested some variations: (1) pure GelMA, (2) GelMA:Matrigel at a ratio of 5:1, (3) GelMA:Matrigel at 2:1, (4) GelMA:Matrigel at 1:1, (5) GelMA:-Matrigel at 1:2, and (6) pure Matrigel. Pure GelMA and GelMA:-Matrigel (5:1) had a higher compressive modulus than the other materials (Figure S2A), which would better maintain the space between bones after surgery for suture regeneration. The tensile strength was also tested, and there was no significant difference between pure GelMA and GelMA:Matrigel (5:1), whereas the remaining four groups were too soft to be measured. After being soaked/rinsed for 3 weeks, the remaining mass of pure GelMA and GelMA:Matrigel (5:1) remained higher than that of other groups (i.e., they had the lowest degradation rate), which would also help prevent suture refusion after surgery (Figure S2B). Diffusional permeability testing showed that pure GelMA and GelMA:Matrigel (5:1) had the lowest diffusional ability, which may help to block intrusion of cytokines, such as angiogenesis factors that could promote bone formation and suture refusion (Figure S2C). Using pure Matrigel, which had the highest diffusional permeability, suture refusion occurred in as soon as 1 month (Figure S3J). The swelling ratio showed results similar to the diffusional permeability testing, which suggested that a solution like blood could more easily get into the pure Matrigel and promote bone formation, whereas there was no significant difference between the other five groups (Figure S2D). Taking all these properties into account, we concluded that pure GelMA and GelMA:Matrigel at a 5:1 ratio have the most favorable properties for suture regeneration. It is important to note that Matrigel, a mouse tumor matrix preparation, may be limited in its application for human use.

We compared GelMA:Matrigel:COL-I at a ratio of 10:2:1 (M-GM) to pure GelMA (GM) and GelMA:Matrigel at a ratio of 5:1 (GM-Ma). Scanning electron microscopy (SEM) (Figure S2F) and cellular viability staining (Figure S2G) showed that cells could spread more easily in GM-Ma and M-GM in three-dimensional culture. After six months, M-GM with MSCs formed a regenerated suture more similar to a natural one (Figures S2H–S2L), which suggested that COL-I could attract osteo-related cells in later stages to form a suitable space (Figures S2J and S2L). None of the crucial material properties were changed significantly by adding COL-I to GM-Ma (Figures S2M–S2P). Ultimately, these results suggest that M-GM provides a suitable environment for MSC-mediated suture regeneration.

To investigate whether Gli1^{+} MSCs retained their stemness after 10 days of culture *in vitro*, a colony-forming assay was performed. Gli1^{+} MSCs formed colonies (Figure S2E) and could differentiate toward osteogenic, chondrogenic, and adipogenic lineages (Zhao et al., 2015), confirming their stemness.

Suture MSCs in M-GM Support Regeneration of Cranial Sutures in *Twist1*$^{+/-}$ Mice

To test whether Gli1^{+} MSCs combined with M-GM can support coronal suture regeneration in *Twist1*$^{+/-}$ mice with bilateral coronal suture fusion (Figures 2A and 2C), we generated a rectangular defect 0.3–0.4 mm wide over each of the fused coronal sutures (Figures 2B and 2D). Gli1^{+} cells with M-GM (M-GM+stem cells (SCs) were implanted into the defect on the right side (Figures 2E and 2F). The defect on the opposite side was (1) left empty or filled with (2) pure M-GM, (3) suture mesenchymal cells from *Gli1-Cre*^{ERT2}*;ROSA26*$^{LoxP\text{-}STOP\text{-}LoxP\text{-}DTA\ \ GFP}$ mice mixed with M-GM (M-GM+diphtheria toxin fragment A (DTA) cells), (4) heat-inactivated Gli1^{+} cells (H-SCs) mixed with M-GM (M-GM+H-SCs), or (5) Gli1^{+} cells mixed with Matrigel (Ma+SCs).

One month after surgery, there was already new bone formation in the blank controls (Figures 2G and 2G1), whereas spaces were found between the two bones filled with M-GM alone or with M-GM+SCs (Figures 2H, 2H1, and 2H2). The bone matured in the blank controls 3 months post-surgery (Figures 2I and 2I1), and the lateral bony edges of defects began to meet in the M-GM group (Figures 2J and 2J1). In contrast, the bone edges

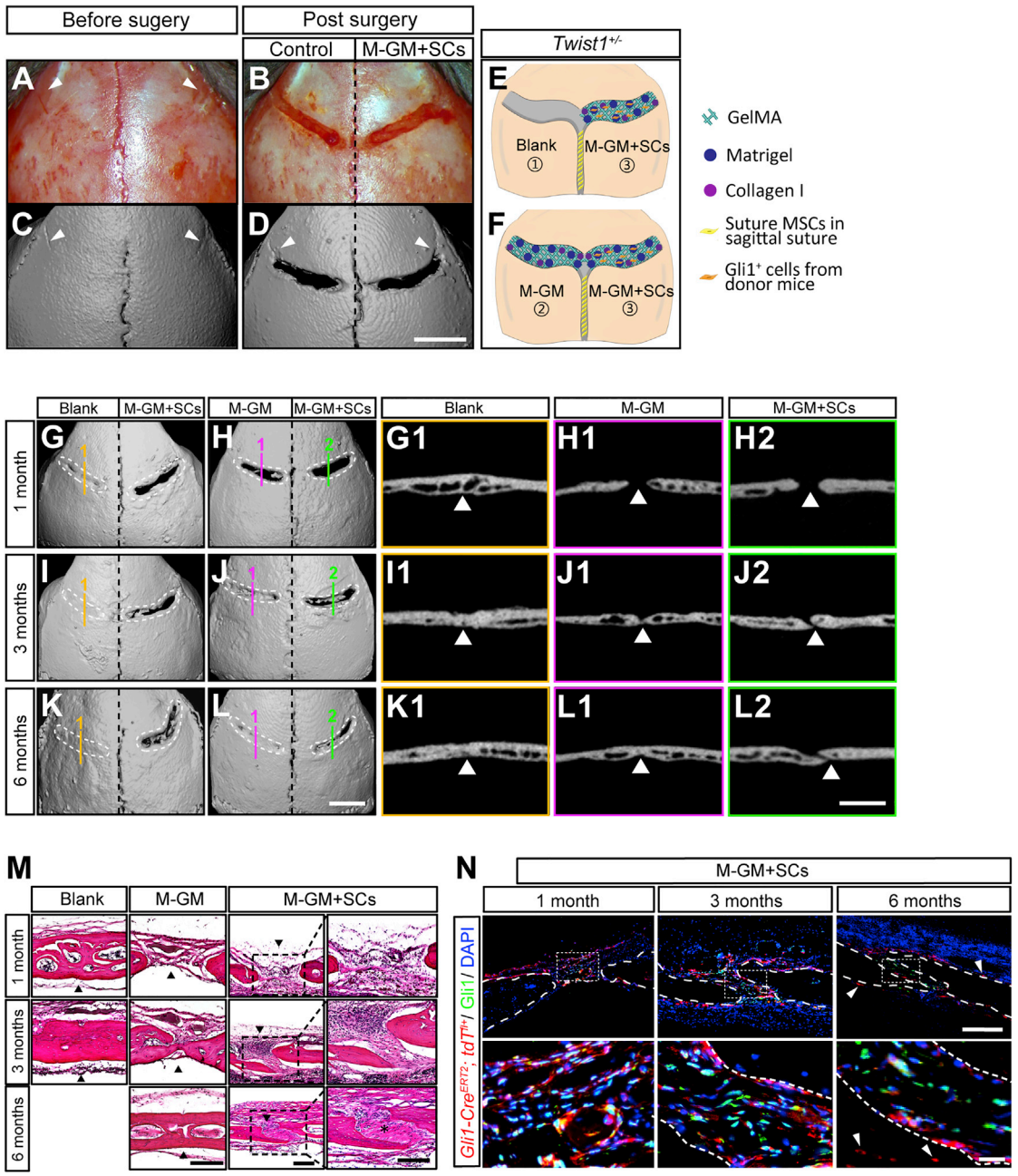

Figure 2. Suture MSCs and M-GM Can Support Regeneration of a Cranial Suture

(A–F) Overview of the calvarial surgery, showing the calvaria before surgery (A and C) and after surgery (B and D) and micro-computed tomography (microCT) of calvaria (C and D). White arrowheads indicate the residual hallmark of the fused suture (A, C, and D). The defect on one side of the calvaria was filled with pure M-GM or left empty as a control, and the defect on the other side was filled with M-GM plus Gli1^{+} cells (E and F). Scale bar, 2 mm.

(G–L) MicroCT images (3D reconstruction and slice) for controls (G1, I1, and K1 for blank and H1, J1, and L1 for pure M-GM) and M-GM plus suture MSCs (M-GM+SCs; H2, J2, and L2) 1, 3, and 6 months post-surgery. Dotted lines (white) outline the original surgical defects. Scale bar, 2 mm.

(M) H&E staining of blank control (left), M-GM (center), and M-GM+SC (right) groups 1, 3, and 6 months post-surgery. The outlined areas in the M-GM+SC group are shown separately in the right panels. Black arrowheads indicate the positions of initial defects, and an asterisk shows suture-like structure in M-GM+SCs 6 months post-surgery. Scale bar, 200 μm.

(N) Immunofluorescence staining for M-GM+SCs 1 month (left), 3 months (center), and 6 months post-surgery (right). Red fluorescently labeled cells were harvested from 1-month-old *Gli1-Cre^{ERT2};tdT$^{fl/+}$* mice. White arrowheads indicate donor cells (red) in surrounding tissues; white dotted lines show boundaries of bones. Scale bars, 200 μm in the top panel and 25 μm in the bottom panel.

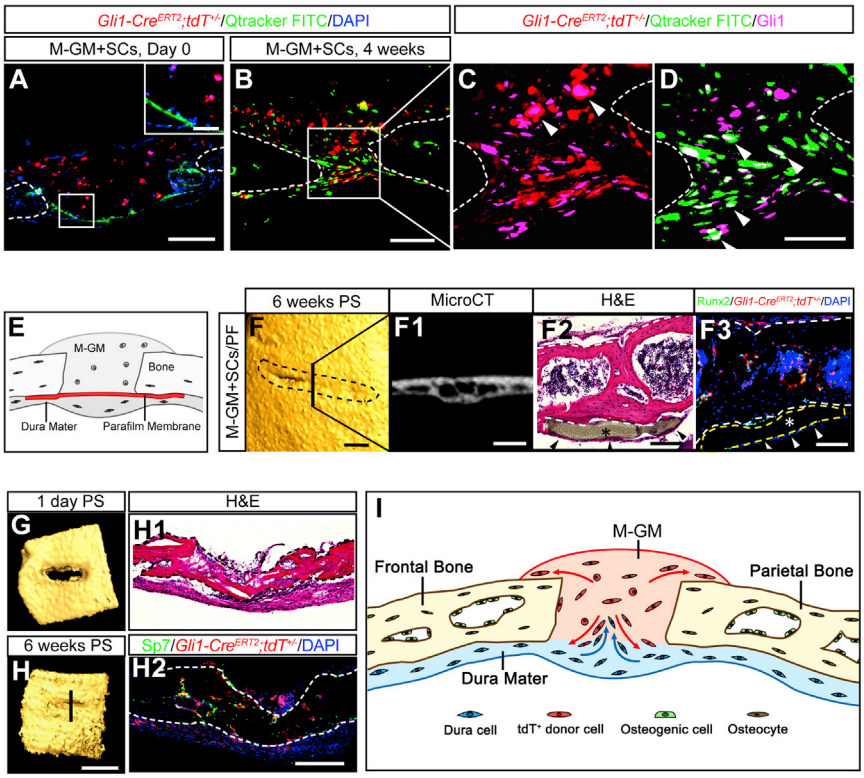

Figure 3. *Dura Mater* Cells Contribute to Regenerated Sutures in *Twist1*$^{+/-}$ Mice

(A–D) Qtracker FITC-labeled (green) *dura mater* cells migrate from the *dura* on day 0 (A) to the regenerated suture 4 weeks post-surgery (B–D). Donor cells fluorescently labeled in red were harvested from 1-month-old *Gli1-Cre*^{ERT2}*;tdT*$^{fl/+}$ mice. Gli1$^+$ cells were labeled with Alexa 647, and arrowheads indicate co-labeled signals (C and D). Scale bars, 50 μm in the inset in (A), 200 μm in (A), 100 μm in (B), and 50 μm in (D).

(E) Schematic of *dura mater* blockage surgery.

(F) MicroCT images (3D reconstruction and slice) and H&E and immunofluorescence staining of the defects 6 weeks post-*dura mater* blocking. Black dotted lines outline the original surgical defects. In (F2) and (F3), Asterisks indicate the Parafilm membrane (yellow dotted lines in F3); arrowheads indicate the *dura mater*. Scale bars, 500 μm in (F) and (F1) and 100 μm in (F2) and (F3).

(G and H) 3D-reconstructed microCT images of bone defects filled with M-GM+MSCs for kidney capsule transplantation 1 day (G) or 6 weeks post-surgery (H). H&E and immunofluorescence staining of the explant is shown in the right panel. Scale bars, 1 mm in (H) and 200 μm in (H1) and (H2).

(I) Schematic drawing showing that M-GM+SCs might provide a niche that recruits endogenous *dura mater* cells into the regenerated suture, whereas donor cells also contribute to self-renewal of surrounding tissues. Bone boundaries are outlined by brown lines.

remained separated in the M-GM+SC group (Figures 2J and 2J2). Six months post-surgery, when the defect was left empty or filled only with M-GM, the suture sites had re-fused (Figures 2K1 and 2L1). At the same time point, the bones were still separated in defects filled with M-GM+SCs (Figures 2K and 2L). Even after 1 year, this regenerated suture remained patent (Figure S3G). All of the other groups experienced resynostosis, including those filled with M-GM+DTA cells (Figure S3H), heat-inactivated M-GM+H-SCs (Figure S3I), and Ma+SCs (Figure S3J), clearly indicating the crucial roles played by live Gli1$^+$ MSCs and M-GM in successful suture regeneration.

Histological analysis (Figure 2M) confirmed disappearance of the coronal suture as well as the presence of thicker bone in the empty defects 1 month post-surgery. In defects filled with M-GM alone, fibrous tissue with some bony islands formed, whereas suture-like tissue could be seen between bone edges in the MGM+SC group. Three months post-surgery, the porous bone structure of the empty defects was replaced by lamellar bone. The bony margins began to connect in the M-GM group and became thicker 6 months post-surgery. In the M-GM+SC group, the gap between the bones remained and new fibrous suture formed within 6 months post-surgery (Figure 2M).

Next we investigated how implanted Gli1$^+$ MSCs may contribute to suture regeneration in *Twist1*$^{+/-}$ mice (Figure 2N). One month post-surgery, the majority of implanted Gli1$^+$ MSCs were present in the center of the defect, whereas a few appeared in the osteogenic fronts, periosteum, and *dura* (Figure 2N, left). Interestingly, in defects filled with M-GM+SCs 3 months post-surgery, large numbers of tdTomato-labeled cells were detectable in the osteogenic fronts, periosteum, and *dura mater* near the suture (Figure 2N, center). A few labeled osteocytes were detected near the osteogenic fronts, whereas some remained in the center of the regenerated suture. Six months post-surgery (Figure 2N, right), progeny of implanted Gli1$^+$ MSCs were detectable in the periosteum, *dura*, and osteocytes of calvaria further away from the defect (white arrowhead), and there were some endogenous Gli1$^+$ MSCs (in green) in the middle of the regenerated suture. Nearly 1 year post-surgery, the majority of the implanted Gli1$^+$ MSCs took part in formation of the nearby tissues, with only a few Gli1$^+$ cells remaining in the center of the suture (Figure S3G). In the defects left empty or filled with M-GM alone, the suture had nearly or totally re-fused, and Runx2$^+$ cells were numerous at all stages (Figures S3E and S3F). These results suggest that the implanted Gli1$^+$ MSCs in the regenerated suture may contribute to turnover of the osteogenic fronts, periosteum, and *dura* to support calvarial tissue homeostasis.

Dura Mater Cells Contribute to Suture Regeneration in *Twist1*$^{+/-}$ Mice

As shown in Figures 2N and S3G, some Gli1$^+$ cells (in green) were present in addition to the implanted Gli1$^+$ MSCs (tdTomato$^+$) in the regenerated suture. The ratio of endogenous to implanted labeled cells increased over time, which suggests that endogenous stem/progenitor cells also played roles in sustaining suture regeneration and function. To investigate the source of these cells, the *dura mater* under the defect was labeled with fluorescein isothiocyanate (FITC) prior to implantation of Gli1$^+$ MSCs and M-GM in *Twist1*$^{+/-}$ mice with craniosynostosis (Figure 3A).

Exogenous and endogenous Gli1$^+$ cells were present in the suture region 4 weeks post-surgery (Figures 3B–3D). To confirm whether MSCs from the *dura* contributed to the newly regenerated suture, a Parafilm membrane with 10-nm pores was placed between the *dura* and the calvarial bone to block migration of endogenous MSCs into the suture (Figure 3E). Six weeks post-surgery, the suture area was almost re-fused in the group with the Parafilm membrane (asterisks in Figures 3F–3F3), in contrast to the group without the Parafilm membrane, in which the suture space was maintained (Figure 2). Kidney capsule transplantation of calvarial explants also indicated that M-GM+MSCs cannot regenerate a suture following removal of the *dura*. The defect in the explanted bone was filled with bone 6 weeks post-transplantation (Figures 3G and 3H–3H2). These data clearly suggest that endogenous Gli1$^+$ MSCs, in conjunction with implanted Gli1$^+$ MSCs, help sustain the regenerated suture in *Twist1*$^{+/-}$ mice (Figure 3I).

Although Twist1 is known to maintain cranial suture MSCs and suture patency during embryonic development, its role in regulating postnatal MSCs in the cranial suture remains unclear. To test the functional requirement of *Twist1* in regulating suture MSC fate in adults, we generated *Gli1CreER;Twist1*$^{fl/fl}$ mice. Loss of *Twist1* in Gli1$^+$ cells did not lead to craniosynostosis in adult *Gli1CreER;Twist1*$^{fl/fl}$ mice (Figures S3O and S3P). This suggests that Twist1's postnatal functions are not essential, which may partially explain why implanted Gli1$^+$ MSCs, together with endogenous *dura*-derived *Twist1*$^{+/-}$ MSCs, can regenerate a sustainable cranial suture and prevent resynostosis in adult *Twist1*$^{+/-}$ mice.

A Regenerated Suture Functions Similarly as a Natural Cranial Suture

To evaluate how functionally similar coronal sutures regenerated by implanted MSCs and M-GM are to natural sutures, we performed RNA sequencing to compare the gene expression profiles of coronal sutures from WT mice, MUT mice, and endogenous cells from *Twist1*$^{+/-}$ mice with regenerated sutures (REG). The WT and MUT groups had distinct gene expression profiles, whereas endogenous cells from the REG group had a gene expression profile more similar to that of a WT coronal suture (Figure 4A). t-distributed stochastic neighbor embedding (t-SNE) analysis confirmed that the gene distributions of WT and endogenous cells from the REG group were closer to each other than to the MUT group (Figure 4B). The WT group and endogenous cells in the REG group had ~3,000 upregulated genes and ~6,000 (WT)/~11,000 (REG) downregulated genes relative to the MUT group, whereas there were only 800–900 differentially expressed genes between the WT group and endogenous cells in the REG group (Figure 4C). Putative marker genes of suture mesenchymal stem/progenitor cells such as *Gli1*, *Prrx1*, and *Axin2* showed increased expression in endogenous cells of the REG group in comparison with the MUT group (Figure 4D). *Msx2*, a gene implicated in osteogenesis (Liu et al., 2019), and *Ostn*, which is specifically expressed in osteoblasts and osteocytes in adult bone (Bord et al., 2005), were upregulated in the MUT group and restored in endogenous cells of the REG group compared with the WT group (Figure 4D). These results suggested that suture regeneration partially restored the normal suture gene expression profile and that exogenous MSCs induced endogenous cells from the *dura* to play an important role in restoring a normal gene expression profile.

To investigate molecular mechanisms underlying suture regeneration, we examined Wnt signaling, which plays an important role in craniosynostosis (Yu et al., 2005). Most genes in the Wnt family were upregulated in the MUT group compared with the endogenous part of the REG group and the WT group (Figure S4C), including *Wnt1*, *Wnt2*, *Wnt3*, *Wnt3a*, *Wnt5a*, and *Wnt9b*, whereas a few were downregulated in the MUT group, such as *Wnt5b*, *Wnt7b*, and *Wnt10b*. Axin2, a negative regulator of Wnt signaling, was downregulated in *Twist1*$^{+/-}$ mice, and its expression was reversed by MSC implantation. These results suggest that *Twist1*$^{+/-}$ cranial sutures exhibited upregulation of Wnt signaling that was reversed by MSC implantation. To examine cellular effects of Wnt signaling upregulation, we assessed the osteogenic differentiation ability of suture mesenchymal cells after treating them with a Wnt activator (Wnt agonist 1) or GSK3 inhibitor (activator of Wnt signaling, LY2090314). Runx2 and osteopontin (OPN) expression levels were significantly increased after Wnt signaling was enhanced (Figures S4A and S4B). The expression levels of Wnt-related genes could be restored by suture regeneration (Figure S4C). These results suggest that Wnt signaling upregulation promotes osteogenic differentiation of suture mesenchymal cells and contributes to craniosynostosis, all of which were reversed by MSC implantation.

To test the stemness of MSCs in the regenerated cranial suture, we harvested suture mesenchymal cells from coronal sutures months post-surgery and demonstrated that these cells were capable of osteogenic, chondrogenic, and adipogenic differentiation (Figure 4E). Interestingly, the tdTomato-labeled donor cells performed poorly in adipogenic differentiation, which implied that these cells were more committed toward osteochondrogenic lineages.

To evaluate the ability of the regenerated suture to repair bone after injury, we created a defect in the parietal bone next to the regenerated coronal suture 6 months after the first surgery (M-GM+SCs group), whereas on the other side of the calvaria, an identical defect was generated in the parietal bone next to the refused coronal suture (where the defect was left empty) (Figures 4F–4H). Three months later, implanted Gli1$^+$ MSCs and endogenous MSCs contributed to bone regeneration (Figures 4K1 and 4K2). The defects initially treated with M-GM+SCs were healed completely (Figure 4I and white asterisk in Figure 4K), whereas the blank controls did not heal fully (white asterisks in Figures 4J and 4J2). These results suggest that regenerating a suture restores its important ability to support tissue regeneration.

To confirm the regeneration and turnover ability of the regenerated suture, we also transplanted calvarial bone containing a newly regenerated suture into another *Twist1*$^{+/-}$ mouse after 6 months (Figures 4L and 4N). Calvarial bone with refused sutures taken from the blank control side of *Twist1*$^{+/-}$ mice with bilateral craniosynostosis was also transplanted as a control (Figures 4L and 4M). Three months later, transplants containing the regenerated suture connected with the host bone (Figures 4O and 4Q). The newly regenerated tissue grew rapidly and doubled in surface area (Figures 4Q1, 4R, and 4S). In contrast, transplants without sutures failed to grow and did not connect with the host bone after

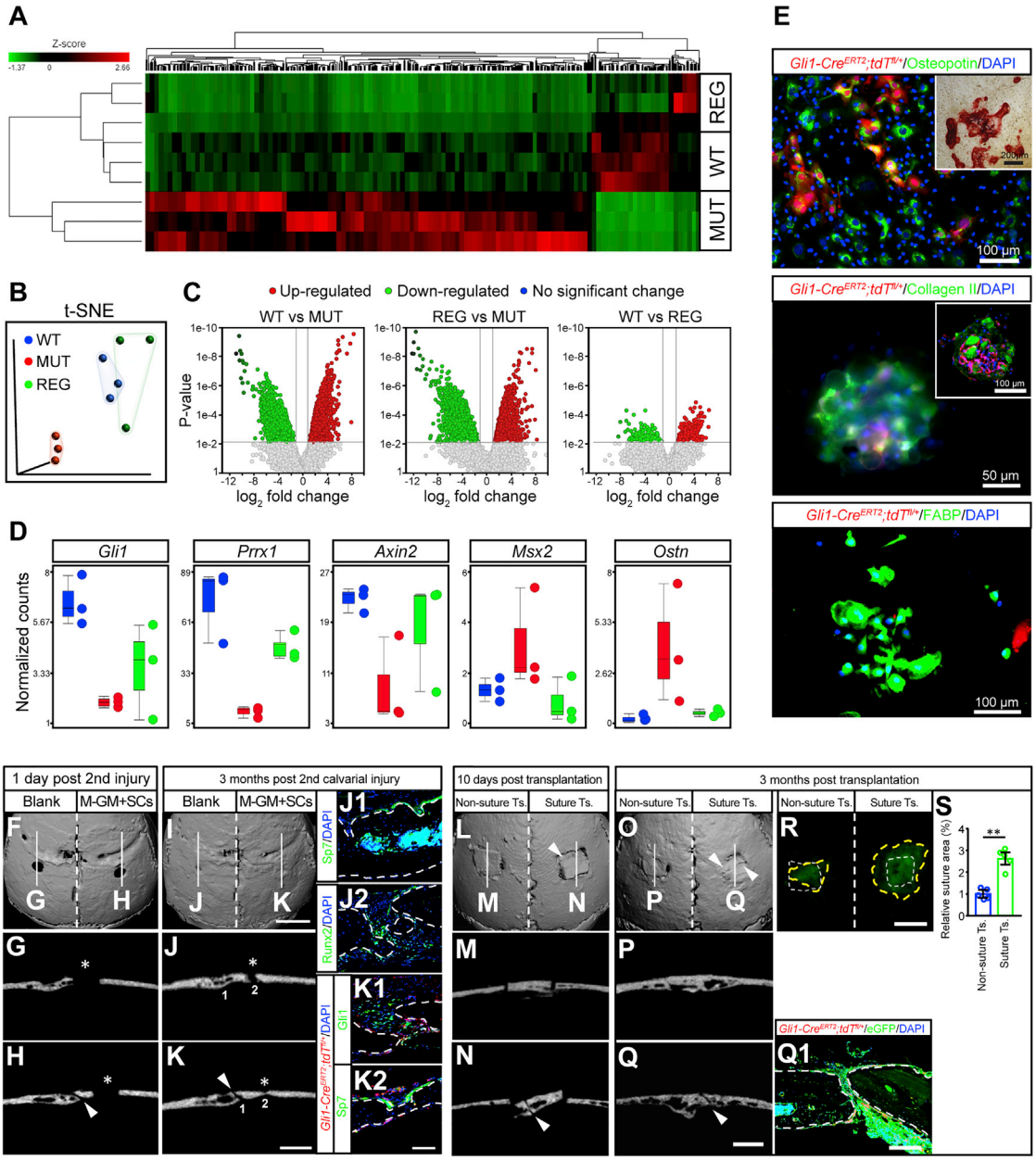

Figure 4. Regenerated Sutures Show a Similar Gene Expression Profile and Function as Natural Cranial Sutures

(A–D) RNA sequencing (ENA-seq) analysis of normal sutures (WT), fused sutures (MUT), and endogenous cells from regenerated sutures (REG). Gene expression profiles are shown with a heatmap (A); t-SNE visualization of color-coded regions for the three groups (B); volcano plots indicating the number of differentially expressed genes (C); and gene signatures of *Gli1*, *Prrx1*, *Axin2*, *Msx2*, and *Ostn* based on the relative expression levels of WT, MUT, and REG (D).

(E) The osteogenic (top panel, alizarin red staining in the inset), chondrogenic (center panel, whole-mount immunostaining and section staining in the inset), and adipogenic (bottom panel) differentiation ability of cells in the regenerated suture.

(F–K) The ability of the regenerated suture to repair bone 1 day (F–H) or 3 months post-injury (I–K). MicroCT slices of blank (G and J) and M-GM+SCs (H and K) sides. Red fluorescently labeled cells were from donor mice (K1 and K2). Asterisks indicate injuries in parietal bones (G, H, J, and K); arrowheads in (H) and (K) indicate the regenerated sutures. Scale bars, 2 mm in (F) and (I); 1 mm in (G), (H), (J), and (K); and 100 μm in (J1), (J2), (K1) and (K2).

(L–S) Visualization 1 day (L–N) and 3 months (O–Q) after transplantation of regenerated sutures or parietal bones without sutures (non-suture transplant) dissected from *CAG-EGFP* mice. Shown are microCT slices of the non-suture transplant group (M and P) and transplants with sutures (N and Q). In (Q1), green fluorescently labeled tissues were from *CAG-EGFP* mice, whereas red cells were from donor *Gli1-Cre*^{ERT2}*;tdT*$^{fl/+}$ mice. Arrowheads indicate the regenerated sutures (L, N, O, and Q). In (R), white dotted lines outline the original size of the transplants, and yellow dotted lines indicate the boundary of the regenerated tissue (R). (S) shows quantification of the fold change of the transplant surface area from (R).

Scale bars, 2 mm in (L), (O), and (R); 1 mm in (M), (N), (P), and (Q); and 200 μm in (Q1). Data are mean ± SEM (S). **$p < 0.01$, calculated by independent two-tailed Student's t test.

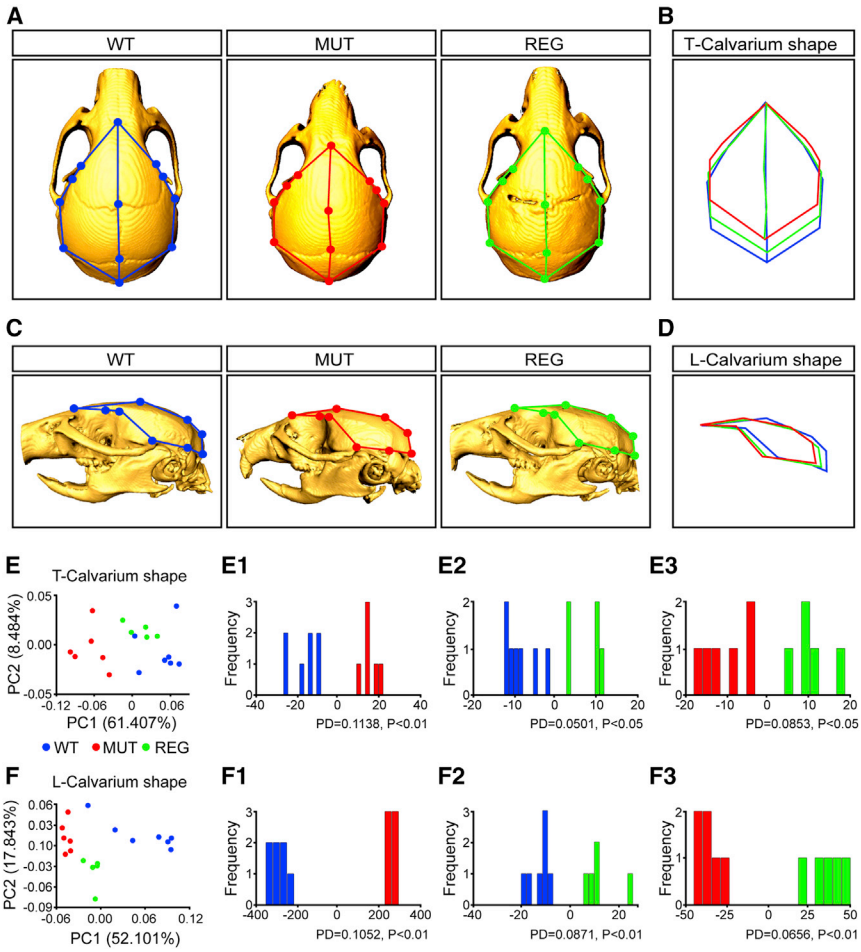

Figure 5. Regenerated Sutures Rescue Skull Deformity in *Twist1*$^{+/-}$ Mice with Craniosynostosis

(A and C) Colored dots indicate landmarks (shown in Figures S7A–S7C) of the top calvarium (T-calvarium) and lateral calvarium (L-calvarium) shape in all three groups; shown are multiple skull views of normal mice (WT, n = 7, blue), MUT mice (n = 6, red), and REG mice (n = 5, green).

(B and D) Wireframe deformations representing the shape differences between the WT, MUT, and REG groups for each region.

(E and F) Total variation between the WT, MUT, and REG groups was determined by principal-component analysis (PCA) for both shape regions. Results of discriminant function analysis (DFA) of three groups for each shape region: top calvarium (E1–E3) and lateral calvarium (F1–F3). Procrustes distance (PD) and p value (*p < 0.05, **p < 0.01) were analyzed for every comparison.

3 months (Figures 4O and 4P). These results indicate that the regenerated suture possesses the important ability to support calvarial bone turnover and homeostasis.

Suture Regeneration Rescues Skull Deformity in *Twist1*$^{+/-}$ Mice

To investigate whether regenerating the suture can correct the skull malformations in *Twist1*$^{+/-}$ mice, we compared the skull shapes of controls (WT), MUT mice, and REG mice. Established anatomical landmarks (Ho et al., 2015; Figures S4D–S4F) were used to analyze the shape of the top of the calvarium (T-calvarium shape; Figure 5B) and the lateral portion of the calvarium (L-calvarium shape; Figure 5D) of each group. Skulls of WT control and REG mice were significantly longer in the anterior-posterior direction than those of MUT mice (Figures 5A and 5C). Principal-component analysis (PCA) revealed that the WT and REG groups were more similar to each other than to the MUT group in T- and L-calvarial shape (Figures 5E and 5F). Although the REG group had a different T-calvarium shape than the WT (Figure 5E2; Procrustes distance = 0.0501, $p < 0.05$), the differences between the MUT and WT/REG groups were greater (Figure 5E1; Procrustes distance = 0.1138, $p < 0.01$ and Figure 5E3; Procrustes distance = 0.0853, $p < 0.01$). The first principal component (PC1) of L-calvarium shape, which accounted for 52.101% of the total variation in the sample, placed REG mice between the other two groups (Figures 5F–5F3). These results indicated that suture regeneration partially rescued head shape deformity in *Twist1*$^{+/-}$ mice with craniosynostosis.

Suture Regeneration Improves Neurocognitive Functions in *Twist1*$^{+/-}$ Mice with Craniosynostosis

To test whether suture regeneration rescues neurocognitive dysfunctions in *Twist1*$^{+/-}$ mice with craniosynostosis, we first created a comparison group by performing bilateral suture regeneration surgery on WT mice on post-natal day 14. The suture structure was recovered 6 weeks post-surgery (Figure S7A) in these mice. We then measured ICP and performed behavioral tests. We did not detect significant changes in ICP (Figure S7B), social recognition (Figures S7C–S7E), motor learning (Figure S7F), or anxiety-related behaviors (Figures S7G and S7H) in recovered WT mice. These results confirmed that the surgical procedure per se does not introduce behavioral changes.

We next confirmed that elevated ICP in *Twist1*$^{+/-}$ mice was restored after suture regeneration (Figures 6A and 6B). We subjected WT and *Twist1*$^{+/-}$ mice with or without suture regeneration to a battery of behavioral tests. The novel object test revealed that the impaired preference for novel objects in *Twist1*$^{+/-}$ mice was restored after suture regeneration (Figures 6D and 6E). The three-chamber test showed that suture regeneration also significantly rescued the sociability and social novelty deficits in *Twist1*$^{+/-}$ mice (Figures 6F–6H). Despite a trend toward improvement, motor learning was not significantly rescued after suture regeneration (Figure 6C). We did not detect changes in general locomotion (Figures S5A and S5B),

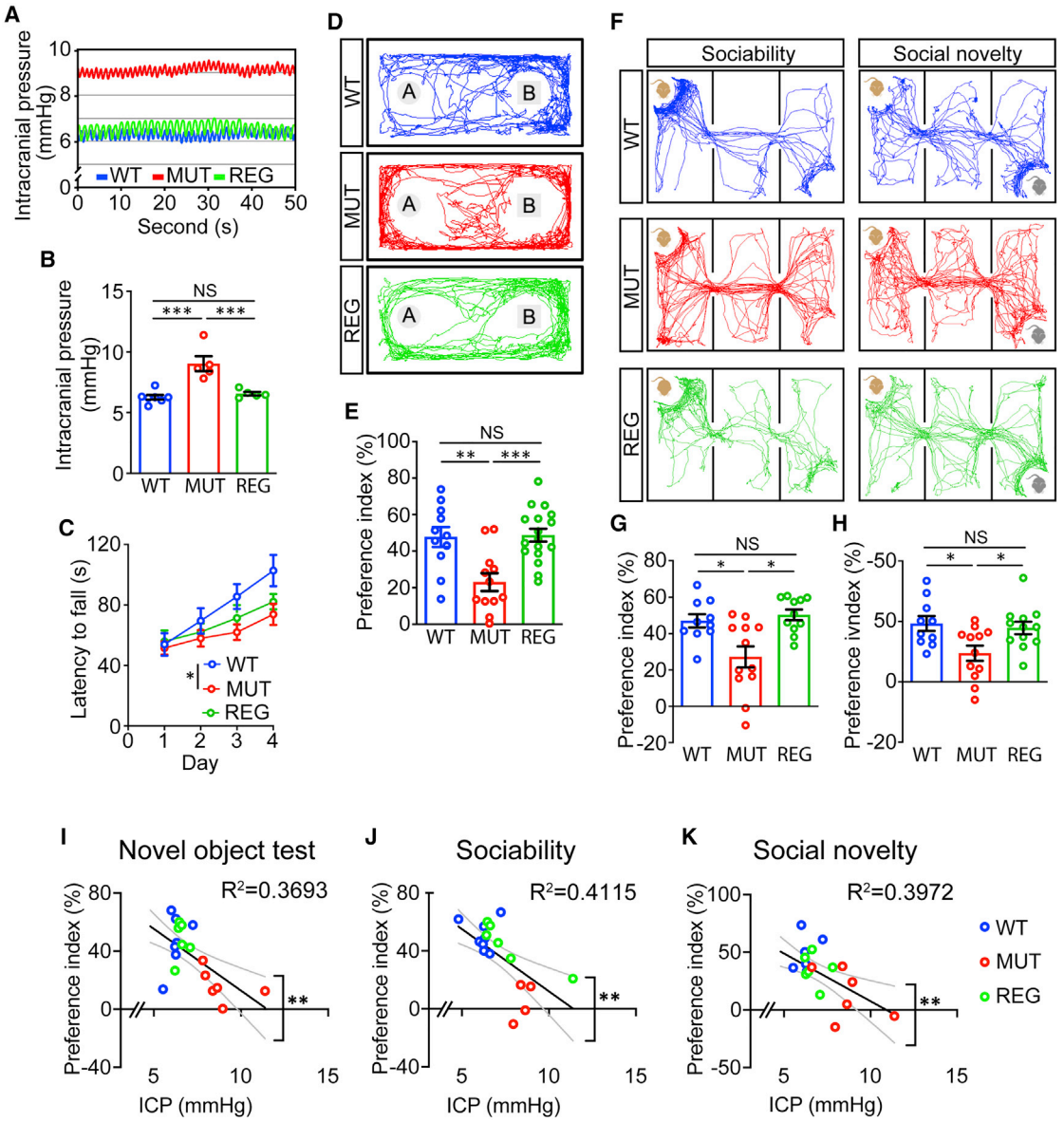

Figure 6. Suture Regeneration Normalizes ICP and Partially Restores Neurocognitive Function in *Twist1*$^{+/-}$ Mice with Craniosynostosis

(A and B) Representative ICP traces (A) and quantification (B) of ICP values (WT, n = 7; MUT, n = 5; REG, n = 5 mice).

(C) Rotarod performance scored as time (seconds) on the rotarod (WT, n = 10; MUT, n = 12; REG, n = 10 mice).

(D and E) Representative animal tracks (D) and preference index (E) of the novel object test (WT, n = 11; MUT, n = 12; REG, n = 17 mice).

(F–H) Representative animal tracks (F) and preference indices of sociability (G) and social novelty (H) in the three-chamber test (WT, n = 10; MUT, n = 12; REG, n = 12 mice).

(I–K) ICP values plotted against preference indices in the novel object test (I) and sociability (J) and social novelty (K) in the three-chamber test (WT, n = 7; MUT, n = 6; REG, n = 6 mice).

Data are mean ± SEM (B, C, E, G, and H). *p < 0.05, **p < 0.01, ***p < 0.001, calculated by one-way ANOVA (B, E, and G) with Tukey post hoc tests and two-tailed unpaired t test (C).

grip strength (Figure S5D), or olfaction (Figures S5H and S5I) or obvious anxiety-related behaviors (Figures S5C and S5E–S5G).

We performed correlation analyses between ICP and cognitive behaviors, including novel object preference, sociability, and social novelty, which were impaired in *Twist1*$^{+/-}$ mice. There was a positive correlation between ICP elevation and behavioral deficits, which was reversed by MSC-mediated suture regeneration (Figures 6I–6K). These results suggested that suture regeneration rescued neurocognitive dysfunctions in *Twist1*$^{+/-}$ mice, likely through reduction of ICP.

To evaluate the importance of surgery timing, we performed suture regeneration surgery on *Twist1*$^{+/-}$ mice at post-natal

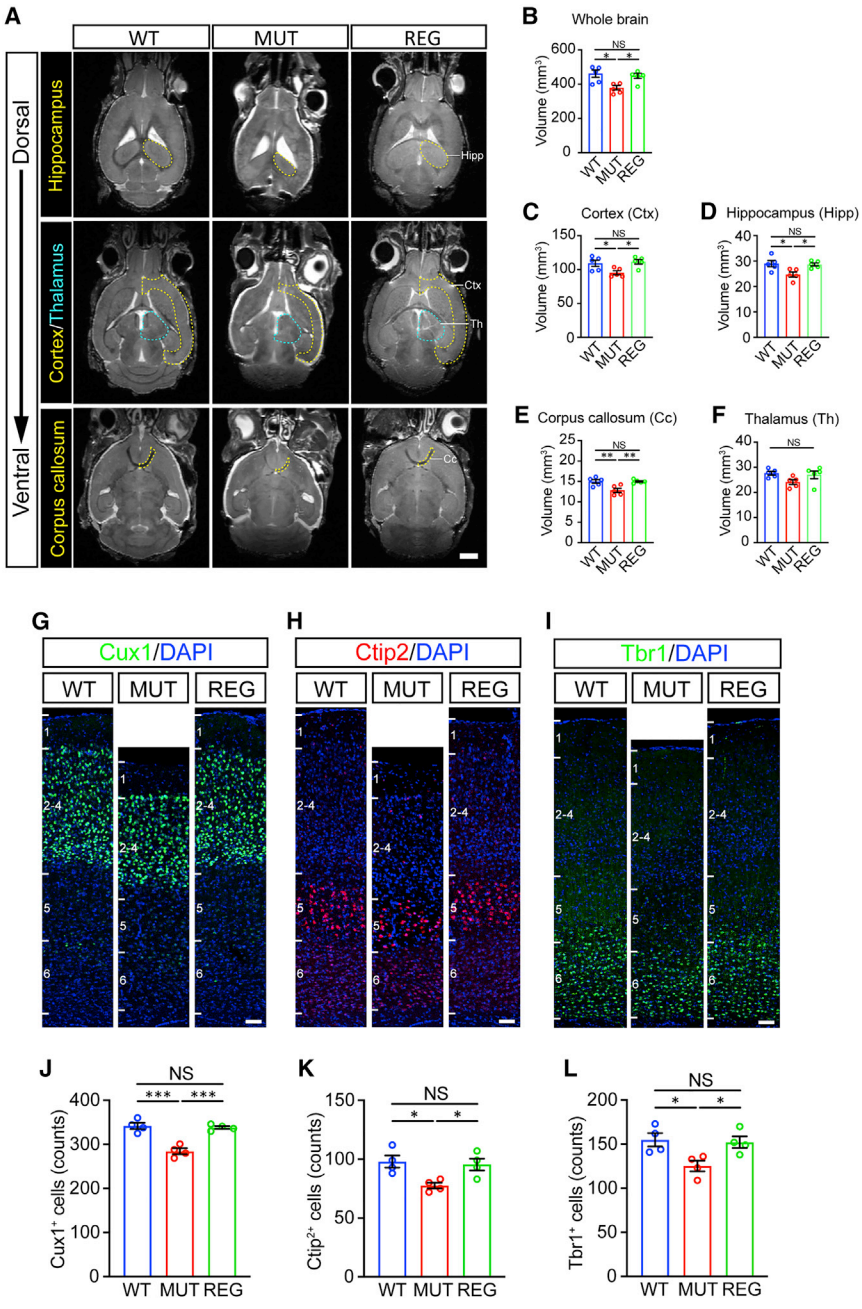

Figure 7. Suture Regeneration Surgery Performed on Post-natal Day 14 Restores Brain Morphology in *Twist1*$^{+/-}$ Mice with Craniosynostosis

(A) Representative magnetic resonance images of WT, MUT, and REG mouse brains. The hippocampus (Hipp), cortex (Ctx), *corpus callosum* (Cc), and thalamus (Th) are outlined by yellow or cyan dotted lines. Scale bar, 2 mm.

(B–F) Quantifications of volume of whole brain (B), Ctx (C), Hipp (D), Cc (E), and thalamus (F) (WT, n = 5; MUT, n = 5; REG, n = 5 mice).

(G–I) Representative images of Cux1$^+$ (G), Ctip2$^+$ (H), and Tbr1$^+$ (I) cells in the somatosensory cortex. Scale bar, 50 μm.

(J–L) Quantification of Cux1$^+$ (J), Ctip2$^+$ (K), and Tbr1$^+$ (L) cells in the somatosensory cortex with 300-μm width (WT, n = 4; MUT, n = 4; REG, n = 4 mice).

*p < 0.05, **p < 0.01, ***p < 0.001, calculated by one-way ANOVA with Tukey post hoc tests.

week 8, which corresponds to an adult human ~20 years old (Semple et al., 2013). Behavioral studies did not detect significant rescue of neurocognitive deficits when surgery was performed at this later age (Figures S6A–S6F), suggesting that the timing of suture regeneration surgery is crucial.

Suture Regeneration Restores Brain Volume and Neural Numbers in *Twist1*$^{+/-}$ Mice with Craniosynostosis

In humans, untreated craniosynostosis can lead to microcephaly (Blount et al., 2007; Kabbani and Raghuveer, 2004; Lane, 1892), correlating with high risk of impaired intelligence, speech, and learning as well as behavioral problems (Shim et al., 2016). To investigate the mechanisms underlying rescue of neurocognitive functions by suture regeneration, we measured brain volume using magnetic resonance imaging (MRI). Consistent with microcephaly in craniosynostosis patients, whole-brain volume was reduced in *Twist1*$^{+/-}$ mice with craniosynostosis, but this was reversed by suture regeneration (Figures 7A and 7B). We then examined specific brain regions involved in behaviors altered in *Twist1*$^{+/-}$ mice with craniosynostosis. The cortical mantle, hippocampus, and *corpus callosum* volumes were reduced significantly reduced in *Twist1*$^{+/-}$ mice and restored after suture regeneration (Figures 7A and 7C–7E), whereas the thalamic volume was not changed significantly in *Twist1*$^{+/-}$ mice (Figures 7A and 7F).

To investigate the cellular basis of brain volume changes, we examined neural numbers in different cortical layers, including Cux1-labeled layer II–IV neurons and Ctip2- and Tbr1- labeled layer V–VI neurons (Leone et al., 2008; Molyneaux et al., 2007). Immunohistochemistry (IHC) staining showed that Cux1$^+$, Ctip2$^+$, and Tbr1$^+$ neurons were all reduced in *Twist1*$^{+/-}$ mice (Figures 7G–7L) and restored after suture regeneration (Figures 7G–7L). This may indicate restored neurogenesis following suture regeneration in *Twist1*$^{+/-}$ mice with craniosynostosis but could also result from reduced cell death. Focusing on the neuronal activation maker c-Fos, we examined prelimbic and perirhinal cortical regions, which are implicated in social and object recognition, respectively (Rinaldi et al., 2008; Krueger et al., 2009; Buckley and Gaffan, 2006). IHC staining showed that the numbers of c-

Fos$^+$ cells were increased in *Twist1*$^{+/-}$ mice and restored to normal levels after suture regeneration (Figure S6G). These results suggest that suture regeneration restored neural numbers and brain volume reduced in *Twist1*$^{+/-}$ mice, providing crucial insights into the mechanisms underlying impairment and restoration of neurocognitive functions.

DISCUSSION

By combining MSCs with biomaterials and establishing a mouse model of neurocognitive defects associated with craniosynostosis, we have discovered that Gli1$^+$ MSC-based cranial suture regeneration restores not only skull dysmorphology but also neurocognitive dysfunctions in the *Twist1*$^{+/-}$ mouse model of craniosynostosis. These findings represent a research paradigm shift and provide a MSC-based therapeutic strategy for treating craniosynostosis with potential beneficial effects on clinical practice.

Mutant animal models have been instrumental in elucidating the molecular and cellular etiology of craniosynostosis. Many of these models phenocopy the synostoses seen in individuals with the same genetic mutation, making them highly valuable (Twigg and Wilkie, 2015). However, nearly all studies have focused exclusively on cranial suture defects; analysis of the ICP and neurocognitive functions of these models has been lacking. Here we established *Twist1*$^{+/-}$ mice to model neuroanatomic and cognitive dysfunction in individuals with craniosynostosis. These findings will promote future research of neurocognitive dysfunction in other craniosynostosis mouse models and lay the foundation for investigating the molecular, cellular, and circuit mechanisms that underlie them. Our discoveries also facilitate design and evaluation of future therapeutic interventions because syndromic and non-syndromic craniosynostosis lead to increased ICP and altered brain morphology, which, in turn, may cause significant changes in neurocognitive function (Bellew et al., 2005; Brooks et al., 2018; Renier et al., 1982; Sidoti et al., 1996). We developed an effective treatment where Gli1$^+$ MSCs and modified GelMA support cranial suture regeneration and correct skull dysmorphology in *Twist1*$^{+/-}$ mice with craniosynostosis. These findings have significant potential clinical value.

Surgical correction of craniosynostosis is performed routinely within the first year of life. Whole-vault cranioplasty and endoscopic synostectomy followed by skull-molding helmet therapy are currently the most common treatments (Brooks et al., 2018). However, these procedures are invasive and associated with resynostosis and other complications. An improved treatment option is needed to ensure long-term quality of life for these young individuals. Our successful MSC-based suture regeneration depends on a uniquely modified GelMA (M-GM) scaffold that is biocompatible with Gli1$^+$ MSCs, biodegradable, and provides excellent support for suture regeneration. Our therapeutic strategy regenerates cranial sutures that remain patent for at least 1 year and continue to function similarly as a natural cranial suture in injury repair and maintaining tissue homeostasis. Our results suggest that MSCs implanted with M-GM are a less invasive and sustainable biological solution for individuals with craniosynostosis.

Our studies provide cellular and molecular insights into the cranial suture regeneration and maintenance processes. We established the importance and inter-dependence of exogenously implanted Gli1$^+$ MSCs and endogenous MSCs derived from the *dura mater* in cranial suture regeneration in *Twist1*$^{+/-}$ mice. This is consistent with the crucial role of multipotent progenitors in the *dura mater* in calvarial tissue homeostasis (Gagan et al., 2007; Kwan et al., 2008; Ogle et al., 2004). MSC grafts can recruit endogenous stem cells to regeneration sites (Xing et al., 2014), likely facilitated by Wnt3a, platelet-derived growth factor (PDGF), and vascular endothelial growth factor (VEGF) (Shin and Peterson, 2013). At the molecular level, haploinsufficiency of *Twist1* leads to compromised Axin2 and elevated Wnt signaling (Yu et al., 2005). Implantation of exogenous MSCs restored Wnt signaling to a level comparable with control samples, preventing resynostosis. Furthermore, our data show that Twist1's postnatal functions are not essential because loss of *Twist1* in Gli1$^+$ MSCs does not lead to craniosynostosis in adult mice. This result also partially explains how implanted MSCs, along with recruited endogenous Gli1$^+$ MSCs, can regenerate a patent cranial suture despite haploinsufficiency of *Twist1*. Our findings suggest that implanted MSCs establish a conducive niche into which there is dynamic recruitment and integration of endogenous MSCs to support regeneration of a functional and sustainable cranial suture.

One major discovery is that restoration of suture patency not only rescues skull deformity but also normalizes ICP and restores neurocognitive function. Individuals with craniosynostosis often have learning disabilities (Kilcoyne et al., 2019; Twigg and Wilkie, 2015; Zechi-Ceide et al., 2012). Non-syndromic craniosynostosis affecting different cranial sutures may have differential effects on neurocognitive function (Sun et al., 2019). Our suture regeneration approach rescued several behavioral abnormalities in *Twist1*$^{+/-}$ mice, including deficits in novel object recognition, sociability, and social novelty. Our studies suggest that elevated ICP causes, at least in part, neurocognitive dysfunction that is rescued by suture regeneration in *Twist1*$^{+/-}$ mice with craniosynostosis. Our MRI and histological studies indicate that changes in neural numbers and brain volume contribute to neurocognitive dysfunction in *Twist1*$^{+/-}$ mice and that these changes are restored following suture regeneration. Our studies provide important insights into the mechanisms underlying improvement of neurocognitive function by suture regeneration. Twist1 is not expressed in the adult mouse brain, and *Twist1*$^{+/-}$ mice without craniosynostosis have normal ICP and neurocognitive function, suggesting that Twist1 does not have a direct role in regulating development and function of brain structures. In humans, however, TWIST1 is expressed in the cerebral cortex during fetal development and upper layer excitatory neurons in adults (Sousa et al., 2017; Zhu et al., 2018). Future studies will elucidate the molecular mediators or neural circuits leading to selective cognitive dysfunction and restoration in different synostosis models.

Our study demonstrates that MSCs combined with M-GM can regenerate a cranial suture, restore normal ICP, and rescue neurocognitive function in a highly clinically relevant craniosynostosis model. There are still challenges for clinical implementation of this approach, such as identifying the optimal timing of surgery

and the ideal source and dosage of MSCs; these will need to be investigated further to maximize therapeutic efficacy. Nevertheless, our cranial suture regeneration approach offers an effective and less invasive treatment option for craniosynostosis, bringing new hope for individuals who suffer from this devastating disease.

STAR★METHODS

Detailed methods are provided in the online version of this paper and include the following:

- KEY RESOURCES TABLE
- RESOURCE AVAILABILITY
  - Lead Contact
  - Materials Availability
  - Data and Code Availability
- EXPERIMENTAL MODEL AND SUBJECT DETAILS
  - Animals
  - Cell culture, sorting and colony-forming assay
- METHOD DETAILS
  - Intracranial pressure measurement
  - Behavioral assays
  - Gel synthesis and testing
  - Morphology and viability of cells in hydrogels
  - Calvarial defect generation
  - Dura mater blocking
  - Kidney capsule transplantation
  - MicroCT imaging
  - Immunofluorescence staining and *in situ* hybridization (ISH)
  - Western blot analysis
  - RNA sequencing analysis
  - Confirmation of suture MSC stemness
  - Calvarial injury model
  - Suture transplantation
  - Craniofacial shape analysis
  - MRI analysis
  - Inclusion and exclusion criteria for mouse behavioral test
- QUANTIFICATION AND STATISTICAL ANALYSIS
  - Statistics and reproducibility

ACKNOWLEDGMENTS

We thank Dr. Bridget Samuels for critical reading of the manuscript. We thank Drs. Robert Maxson, Pedro Sanchez, and Scott Fraser for *Twist1*$^{+/-}$ and *Twist1*$^{fl/fl}$ mice and discussions. This study was supported by grants from the National Institute of Dental and Craniofacial Research, National Institute of Health (R01 DE026339, R01 DE012711, R01 DE022503, and U24 026914 to Y.C.) and from the National Institute of Neurological Disorders and Stroke, National Institute of Health (R01 NS097231 to J.-F.C.).

AUTHOR CONTRIBUTIONS

M.Y. and Y.C. designed the study. M.Y., L.M., and Y.Y. carried out most of the experiments. X.Y. and H.W. participated in biomaterial synthesis and testing. A.M., N.S.M., R.J., and B.V.Z. designed and participated in the MRI analysis. J.H. participated in analysis of adult *Gli1Cre*^{ER};*Twist1*$^{fl/fl}$ mice. T.-V.H. participated in the microCT analysis. Y.W. participated in intracranial pressure measurement. M.Y. and L.M. analyzed all data. J.-F.C., M.U., and Z.Z. provided comments. M.Y., L.M., J.-F.C., and Y.C. co-wrote the paper. Y.C. supervised the research.

DECLARATION OF INTERESTS

The authors declare no competing interests.

Received: March 16, 2020
Revised: July 28, 2020
Accepted: November 16, 2020
Published: January 7, 2021

REFERENCES

Arbuckle, E.P., Smith, G.D., Gomez, M.C., and Lugo, J.N. (2015). Testing for Odor Discrimination and Habituation in Mice. J. Vis. Exp. *99*, e52615.

Bellew, M., Chumas, P., Mueller, R., Liddington, M., and Russell, J. (2005). Pre- and postoperative developmental attainment in sagittal synostosis. Arch. Dis. Child. *90*, 346–350.

Bildsoe, H., Loebel, D.A., Jones, V.J., Chen, Y.T., Behringer, R.R., and Tam, P.P. (2009). Requirement for Twist1 in frontonasal and skull vault development in the mouse embryo. Dev. Biol. *331*, 176–188.

Blount, J.P., Louis, R.G., Tubbs, R.S., and Grant, J.H. (2007). Pansynostosis: a review. Childs Nerv. Syst. *23*, 1103–1109.

Bord, S., Ireland, D.C., Moffatt, P., Thomas, G.P., and Compston, J.E. (2005). Characterization of osteocrin expression in human bone. J. Histochem. Cytochem. *53*, 1181–1187.

Brooks, E.D., Beckett, J.S., Yang, J., Timberlake, A.T., Sun, A.H., Chuang, C., and Persing, J.A. (2018). The Etiology of Neuronal Development in Craniosynostosis: A Working Hypothesis. J. Craniofac. Surg. *29*, 49–55.

Buckley, M.J., and Gaffan, D. (2006). Perirhinal cortical contributions to object perception. Trends Cogn. Sci. *10*, 100–107.

Cabe, P.A., Tilson, H.A., Mitchell, C.L., and Dennis, R. (1978). A simple recording grip strength device. Pharmacol. Biochem. Behav. *8*, 101–102.

Chan, C.K.F., Gulati, G.S., Sinha, R., Tompkins, J.V., Lopez, M., Carter, A.C., Ransom, R.C., Reinisch, A., Wearda, T., Murphy, M., et al. (2018). Identification of the Human Skeletal Stem Cell. Cell *175*, 43–56.e21.

Chen, Z.F., and Behringer, R.R. (1995). Twist is required in head mesenchyme for cranial neural tube morphogenesis. Genes Dev. *9*, 686–699.

Collett, B.R., Kapp-Simon, K.A., Wallace, E., Cradock, M.M., Buono, L., and Speltz, M.L. (2017). Attention and executive function in children with and without single-suture craniosynostosis. Child Neuropsychol. *23*, 83–98.

Cowan, C.M., Shi, Y.Y., Aalami, O.O., Chou, Y.F., Mari, C., Thomas, R., Quarto, N., Contag, C.H., Wu, B., and Longaker, M.T. (2004). Adipose-derived adult stromal cells heal critical-size mouse calvarial defects. Nat. Biotechnol. *22*, 560–567.

Gagan, J.R., Tholpady, S.S., and Ogle, R.C. (2007). Cellular dynamics and tissue interactions of the dura mater during head development. Birth Defects Res. C Embryo Today *81*, 297–304.

Gompers, A., Su-Feher, L., Ellegood, J., Copping, N.A., Riyadh, M.A., Stradleigh, T.W., Pride, M.C., Schaffler, M.D., Wade, A.A., Catta-Preta, R., et al. (2017). Germline Chd8 haploinsufficiency alters brain development in mouse. Nat. Neurosci. *20*, 1062–1073.

Gripp, K.W., Zackai, E.H., and Stolle, C.A. (2000). Mutations in the human TWIST gene. Hum. Mutat. *15*, 479.

Guo, Y., Yuan, Y., Wu, L., Ho, T.V., Jing, J., Sugii, H., Li, J., Han, X., Feng, J., Guo, C., and Chai, Y. (2018). BMP-IHH-mediated interplay between mesenchymal stem cells and osteoclasts supports calvarial bone homeostasis and repair. Bone Res. *6*, 30.

Habeeb, A.F. (1966). Determination of free amino groups in proteins by trinitrobenzenesulfonic acid. Anal. Biochem. *14*, 328–336.

Ho, T.V., Iwata, J., Ho, H.A., Grimes, W.C., Park, S., Sanchez-Lara, P.A., and Chai, Y. (2015). Integration of comprehensive 3D microCT and signaling analysis reveals differential regulatory mechanisms of craniofacial bone development. Dev. Biol. *400*, 180–190.

Holmes, A., Wrenn, C.C., Harris, A.P., Thayer, K., and Crawley, J.N. (2002a). Behavioral profiles of inbred strains on novel, olfactory, spatial and emotional tests for reference memory in mice. Genes Brain Behav. *1*, 55–69.

Holmes, A., Yang, R.J., and Crawley, J.N. (2002b). Evaluation of an anxiety-related phenotype in galanin overexpressing transgenic mice. J. Mol. Neurosci. *18*, 151–165.

James, A.W., Xu, Y., Wang, R., and Longaker, M.T. (2008). Proliferation, osteogenic differentiation, and fgf-2 modulation of posterofrontal/sagittal suture-derived mesenchymal cells in vitro. Plast. Reconstr. Surg. *122*, 53–63.

Kabbani, H., and Raghuveer, T.S. (2004). Craniosynostosis. Am. Fam. Physician *69*, 2863–2870.

Kaemmerer, E., Melchels, F.P., Holzapfel, B.M., Meckel, T., Hutmacher, D.W., and Loessner, D. (2014). Gelatinemethacrylamide-based hydrogels: an alternative three-dimensional cancer cell culture system. Acta Biomater. *10*, 2551–2562.

Kang, M., Day, C.A., Kenworthy, A.K., and DiBenedetto, E. (2012). Simplified equation to extract diffusion coefficients from confocal FRAP data. Traffic *13*, 1589–1600.

Kilcoyne, S., Luscombe, C., Scully, P., Jayamohan, J., Magdum, S., Wall, S., Johnson, D., and Wilkie, A.O.M. (2019). Language Development, Hearing Loss, and Intracranial Hypertension in Children With TWIST1-Confirmed Saethre-Chotzen Syndrome. J. Craniofac. Surg. *30*, 1506–1511.

Klingenberg, C.P. (2011). MorphoJ: an integrated software package for geometric morphometrics. Mol. Ecol. Resour. *11*, 353–357.

Krueger, F., Barbey, A.K., and Grafman, J. (2009). The medial prefrontal cortex mediates social event knowledge. Trends Cogn. Sci. *13*, 103–109.

Kwan, M.D., Wan, D.C., Wang, Z., Gupta, D.M., Slater, B.J., and Longaker, M.T. (2008). Microarray analysis of the role of regional dura mater in cranial suture fate. Plast. Reconstr. Surg. *122*, 389–399.

Lane, L.C. (1892). Pioneer Craniectomy for Relief of Mental Imbecility Due to Premature Sutural Closure and Microcephalus. JAMA *18*, 49–50.

Leger, M., Quiedeville, A., Bouet, V., Haelewyn, B., Boulouard, M., Schumann-Bard, P., and Freret, T. (2013). Object recognition test in mice. Nat. Protoc. *8*, 2531–2537.

Leone, D.P., Srinivasan, K., Chen, B., Alcamo, E., and McConnell, S.K. (2008). The determination of projection neuron identity in the developing cerebral cortex. Curr. Opin. Neurobiol. *18*, 28–35.

Liu, Y., Wang, L., Kikuiri, T., Akiyama, K., Chen, C., Xu, X., Yang, R., Chen, W., Wang, S., and Shi, S. (2011). Mesenchymal stem cell-based tissue regeneration is governed by recipient T lymphocytes via IFN-gamma and TNF-alpha. Nat. Med. *17*, 1594–1601.

Liu, H., Chen, B., and Li, Y. (2019). microRNA-203 promotes proliferation, differentiation, and migration of osteoblasts by upregulation of Msh homeobox 2. J. Cell. Physiol. *234*, 17639–17648.

Mao, J.J., Giannobile, W.V., Helms, J.A., Hollister, S.J., Krebsbach, P.H., Longaker, M.T., and Shi, S. (2006). Craniofacial tissue engineering by stem cells. J. Dent. Res. *85*, 966–979.

Maruyama, T., Jeong, J., Sheu, T.J., and Hsu, W. (2016). Stem cells of the suture mesenchyme in craniofacial bone development, repair and regeneration. Nat. Commun. *7*, 10526.

Millichap, J.G. (2015). Cognitive Development of Children with Craniosynostosis. Pediatr. Neurol. Briefs *29*, 47.

Molyneaux, B.J., Arlotta, P., Menezes, J.R., and Macklis, J.D. (2007). Neuronal subtype specification in the cerebral cortex. Nat. Rev. Neurosci. *8*, 427–437.

Morriss-Kay, G.M., and Wilkie, A.O. (2005). Growth of the normal skull vault and its alteration in craniosynostosis: insights from human genetics and experimental studies. J. Anat. *207*, 637–653.

Murtha, L., McLeod, D., and Spratt, N. (2012). Epidural intracranial pressure measurement in rats using a fiber-optic pressure transducer. J. Vis. Exp. *62*, e3689.

Noshadi, I., Hong, S., Sullivan, K.E., Shirzaei Sani, E., Portillo-Lara, R., Tamayol, A., Shin, S.R., Gao, A.E., Stoppel, W.L., Black, L.D., III., et al. (2017). In vitro and in vivo analysis of visible light crosslinkable gelatin methacryloyl (GelMA) hydrogels. Biomater. Sci. *5*, 2093–2105.

Ogle, R.C., Tholpady, S.S., McGlynn, K.A., and Ogle, R.A. (2004). Regulation of cranial suture morphogenesis. Cells Tissues Organs *176*, 54–66.

Park, S., Zhao, H., Urata, M., and Chai, Y. (2016). Sutures Possess Strong Regenerative Capacity for Calvarial Bone Injury. Stem Cells Dev. *25*, 1801–1807.

Parsons, T.E., Weinberg, S.M., Khaksarfard, K., Howie, R.N., Elsalanty, M., Yu, J.C., and Cray, J.J. (2014). Craniofacial shape variation in Twist1+/− mutant mice. Anat. Rec. (Hoboken) *297*, 826–833.

Reardon, W., Wilkes, D., Rutland, P., Pulleyn, L.J., Malcolm, S., Dean, J.C., Evans, R.D., Jones, B.M., Hayward, R., Hall, C.M., et al. (1997). Craniosynostosis associated with FGFR3 pro250arg mutation results in a range of clinical presentations including unisutural sporadic craniosynostosis. J. Med. Genet. *34*, 632–636.

Renier, D., Sainte-Rose, C., Marchac, D., and Hirsch, J.F. (1982). Intracranial pressure in craniostenosis. J. Neurosurg. *57*, 370–377.

Rinaldi, T., Perrodin, C., and Markram, H. (2008). Hyper-connectivity and hyper-plasticity in the medial prefrontal cortex in the valproic Acid animal model of autism. Front. Neural Circuits *2*, 4.

Semple, B.D., Blomgren, K., Gimlin, K., Ferriero, D.M., and Noble-Haeusslein, L.J. (2013). Brain development in rodents and humans: Identifying benchmarks of maturation and vulnerability to injury across species. Prog. Neurobiol. *106-107*, 1–16.

Shim, K.W., Park, E.K., Kim, J.S., Kim, Y.O., and Kim, D.S. (2016). Neurodevelopmental Problems in Non-Syndromic Craniosynostosis. J. Korean Neurosurg. Soc. *59*, 242–246.

Shin, L., and Peterson, D.A. (2013). Human mesenchymal stem cell grafts enhance normal and impaired wound healing by recruiting existing endogenous tissue stem/progenitor cells. Stem Cells Transl. Med. *2*, 33–42.

Sidoti, E.J., Jr., Marsh, J.L., Marty-Grames, L., and Noetzel, M.J. (1996). Long-term studies of metopic synostosis: frequency of cognitive impairment and behavioral disturbances. Plast. Reconstr. Surg. *97*, 276–281.

Smith, J.P., Hicks, P.S., Ortiz, L.R., Martinez, M.J., and Mandler, R.N. (1995). Quantitative measurement of muscle strength in the mouse. J. Neurosci. Methods *62*, 15–19.

Sousa, A.M.M., Zhu, Y., Raghanti, M.A., Kitchen, R.R., Onorati, M., Tebbenkamp, A.T.N., Stutz, B., Meyer, K.A., Li, M., Kawasawa, Y.I., et al. (2017). Molecular and cellular reorganization of neural circuits in the human lineage. Science *358*, 1027–1032.

Speltz, M.L., Collett, B.R., Wallace, E.R., Starr, J.R., Cradock, M.M., Buono, L., Cunningham, M., and Kapp-Simon, K. (2015). Intellectual and academic functioning of school-age children with single-suture craniosynostosis. Pediatrics *135*, e615–e623.

Sun, A.H., Eilbott, J., Chuang, C., Yang, J.F., Brooks, E.D., Beckett, J., Steinbacher, D.M., Pelphrey, K., and Persing, J.A. (2019). An Investigation of Brain Functional Connectivity by Form of Craniosynostosis. J. Craniofac. Surg. *30*, 1719–1723.

Twigg, S.R., and Wilkie, A.O. (2015). A Genetic-Pathophysiological Framework for Craniosynostosis. Am. J. Hum. Genet. *97*, 359–377.

Van Den Bulcke, A.I., Bogdanov, B., De Rooze, N., Schacht, E.H., Cornelissen, M., and Berghmans, H. (2000). Structural and rheological properties of methacrylamide modified gelatin hydrogels. Biomacromolecules *1*, 31–38.

Wallace, E.R., Collett, B.R., Kapp-Simon, K., Starr, J.R., Birgfeld, C., and Speltz, M.L. (2016). Visuomotor Function in School-Age Children with Single-Suture Craniosynostosis. J. Dev. Behav. Pediatr. *37*, 483–490.

Wolfswinkel, E.M., Howell, L.K., Fahradyan, A., Azadgoli, B., McComb, J.G., and Urata, M.M. (2017). Is Postoperative Intensive Care Unit Care Necessary

following Cranial Vault Remodeling for Sagittal Synostosis? Plast. Reconstr. Surg. *140*, 1235–1239.

Xing, J., Hou, T., Jin, H., Luo, F., Change, Z., Li, Z., Xie, Z., and Xu, J. (2014). Inflammatory microenvironment changes the secretory profile of mesenchymal stem cells to recruit mesenchymal stem cells. Cell. Physiol. Biochem. *33*, 905–919.

Xu, X., Bringas, P., Jr., Soriano, P., and Chai, Y. (2005). PDGFR-alpha signaling is critical for tooth cusp and palate morphogenesis. Dev. Dyn. *232*, 75–84.

Yu, H.M., Jerchow, B., Sheu, T.J., Liu, B., Costantini, F., Puzas, J.E., Birchmeier, W., and Hsu, W. (2005). The role of Axin2 in calvarial morphogenesis and craniosynostosis. Development *132*, 1995–2005.

Zechi-Ceide, R.M., Rodrigues, M.G., Jehee, F.S., Kokitsu-Nakata, N.M., Passos-Bueno, M.R., and Guion-Almeida, M.L. (2012). Saethre-Chotzen phenotype with learning disability and hyper IgE phenotype in a patient due to complex chromosomal rearrangement involving chromosomes 3 and 7. Am. J. Med. Genet. A. *158A*, 1680–1685.

Zhao, H., and Chai, Y. (2015). Stem Cells in Teeth and Craniofacial Bones. J. Dent. Res. *94*, 1495–1501.

Zhao, H., Feng, J., Ho, T.V., Grimes, W., Urata, M., and Chai, Y. (2015). The suture provides a niche for mesenchymal stem cells of craniofacial bones. Nat. Cell Biol. *17*, 386–396.

Zhu, Y., Sousa, A.M.M., Gao, T., Skarica, M., Li, M., Santpere, G., Esteller-Cucala, P., Juan, D., Ferrández-Peral, L., Gulden, F.O., et al. (2018). Spatiotemporal transcriptomic divergence across human and macaque brain development. Science *362*, eaat8077.

STAR★METHODS

KEY RESOURCES TABLE

REAGENT or RESOURCE	SOURCE	IDENTIFIER
Antibodies		
Rabbit polyclonal anti-Gli1	Novus Biological	Cat#NBP1-78259; RRID: AB_11030198
Rabbit monoclonal anti-Runx2 (D1L7F)	Cell Signaling Technology	Cat#12556; RRID: AB_2732805
Rabbit polyclonal anti-Sp7	Abcam	Cat#ab22552; RRID: AB_2194492
Mouse monoclonal anti-Cux1 (B10)	Santa Cruz Biotechnology	Cat#SC514008; RRID: AB_2715519
Rat monoclonal anti-Ctip2 (25B6)	Abcam	Cat#ab18465; RRID: AB_2064130
Rabbit polyclonal anti-Tbr1	Abcam	Cat#ab31940; RRID: AB_2200219
Rabbit monoclonal anti-c-Fos (9F6)	Cell Signaling Technology	Cat#2250; RRID: AB_2247211
Rabbit polyclonal anti-Osteopontin	Abcam	Cat#ab63856; RRID: AB_1524127
Mouse monoclonal anti-beta Actin	Abcam	Cat#ab20272; RRID: AB_445482
Goat anti-rabbit IgG (H+L)	Invitrogen	Cat#A-11008; RRID: AB_143165
Donkey anti-goat IgG (H+L)	Invitrogen	Cat#A-32814; RRID: AB_2762838
Donkey anti-sheep IgG (H+L)	Invitrogen	Cat#A-11015; RRID: AB_141362
Donkey anti-rabbit IgG (H+L)	Invitrogen	Cat#A32795; RRID: AB_2762835
Goat anti-chicken IgG (H+L)	Invitrogen	Cat#A-11039; RRID: AB_142924
Chemicals, Peptides, and Recombinant Proteins		
Matrigel	Corning	Cat#8015323
Collagen I	GIBCO	Cat#A10483-01
Wnt agonist 1	Selleck Chemicals	Cat#S8178; CAS: 2095432-75-8
LY2090314	Selleck Chemicals	Cat#S7063; CAS: 603288-22-8
Loading buffer	Cell Signaling Technology	Cat#7723S
Protease inhibitor	Thermo Fisher Scientific	Cat#1861278
DTT	Cell Signaling Technology	Cat#7723S
Collagenase type I	Worthington	Cat#LS004194
DispaseII	Roche	Cat#04942078001
Heparin	Sigma	Cat#H3149
Critical Commercial Assays		
Mouse Mesenchymal Stem Cell Functional Identification Kit	R&D systems	Cat#SC010
Qtracker 525 Cell Labeling Kit	Thermo Fisher Scientific	Cat#Q25041MP
RNAscope 2.5 HD Chromogenic Assay	ACD	Cat#322360
RNeasy Micro Kit	QIAGEN	Cat#74004
Deposited Data		
Raw and analyzed data	This paper	GEO: GSE155562
Experimental Models: Organisms/Strains		
Mouse: *Twist1*$^{+/-}$	Chen and Behringer, 1995	N/A
Mouse: *Twist1*$^{fl/fl}$	Bildsoe et al., 2009	N/A
Mouse: *Gli1-Cre*^{ERT2}	The Jackson Laboratory	JAX: 007913
Mouse: *ROSA26*$^{LoxP\text{-}STOP\text{-}LoxP\text{-}tdTomato}$	The Jackson Laboratory	JAX: 007905
Mouse: *CAG-EGFP*	The Jackson Laboratory	JAX: 006567
Mouse: *ROSA26*$^{LoxP\text{-}STOP\text{-}LoxP\text{-}eGFP\text{-}DTA}$	The Jackson Laboratory	JAX: 006331
Mouse: C57BL/6J	The Jackson Laboratory	JAX: 000664

(*Continued on next page*)

Continued		
REAGENT or RESOURCE	SOURCE	IDENTIFIER
Software and Algorithms		
Evolution	FISO Technologies	N/A
Smart v3.0	Panlab	https://www.panlab.com/en/products/smart-video-tracking-software-panlab
MATLAB	Kaemmerer et al., 2014	https://www.mathworks.com/products/matlab.html
Leica LAS AF	Leica	N/A
AVIZO 9.4.0	ThermalFisher	N/A
ImageJ	Imagej.net	N/A
Partek flow	Partek	N/A
MorphoJ	Parsons et al., 2014	N/A

RESOURCE AVAILABILITY

Lead Contact

Additional information and requests for resources and reagents should be directed to and will be fulfilled in a timely fashion by the Lead Contact, Yang Chai (ychai@usc.edu).

Materials Availability

Twist1$^{+/-}$ and *Twist1*$^{fl/fl}$ mice are available upon request, subject to approval from the laboratory where these mice were originally generated, and may require a Materials Transfer Agreement. This study did not generate new unique reagents.

Data and Code Availability

RNA sequencing data from seven-month-old control (WT), *Twist1*$^{+/-}$ mice (MUT), and *Twist1*$^{+/-}$ mice at six months post-surgery (suture regeneration group, REG) have been deposited at GEO: GSE155562 [NCBI tracking system #21160175].

EXPERIMENTAL MODEL AND SUBJECT DETAILS

Animals

Twist1$^{+/-}$ and *Twist1*$^{fl/fl}$ mice were obtained from Dr. Robert Maxson (University of Southern California; Chen and Behringer, 1995; Bildsoe et al., 2009). The following strains were purchased from the Jackson Laboratory: *Gli1-Cre*^{ERT2} (JAX no. 007913), *ROSA26*$^{LoxP\text{-}STOP\text{-}LoxP\text{-}tdTomato}$ (JAX no. 007905), *CAG-EGFP* (JAX no. 006567), *ROSA26*$^{LoxP\text{-}STOP\text{-}LoxP\text{-}eGFP\text{-}DTA}$ (JAX no. 006331), and C57BL/6J (JAX no. 000664). For the aged group, mice of both sexes were purchased at about six months of age, and the younger group were two months of age. Mouse experiments were approved by the University of Southern California Institutional Animal Care and Use Committee and performed following the regulations for animal experiments. All mice were housed under a 12 h light/dark cycle in pathogen-free conditions with free access to food and water, in accordance with the Guide for Care and Use of Laboratory Animals of the National Institutes of Health. All mice used in our study were healthy and were not involved in previous procedures. All the mice were identified by ear tags. Ear biopsies were lysed at 55°C overnight in DirectPCR solution (Viagen, 102-T) followed by 85°C heat inactivation for 1 hour and PCR-based genotyping (GoTaq Green Master Mix, Promega, and C1000 Touch Cycler, Bio-rad). Mice were euthanized by carbon dioxide overdose and then decapitation.

For all experiments, mice of both sexes were used. For the experiments in Figures 1 and S1, two-month-old C57BL/6J mice and *Twist1*$^{+/-}$ mice were used for ICP and behavioral assays, and one-month-old C57BL/6J mice were used for *in situ* hybridization of *Twist1*. For the experiments in Figures 2, 3, 4, S2H–S2L, and S3E–S3J, surgeries were performed on *Twist1*$^{+/-}$ mice with bilateral coronal suture fusion at one month of age. Fusion was assessed prior to surgery by live micro-CT (Figures S3K–S3N). For experiments in Figures 4F–4K, a second calvarial defect was made on both sides of the parietal bones six months after suture regeneration in the same *Twist1*$^{+/-}$ mice. For experiments in Figures 4L–4S, suture and bone transplants were obtained from *CAG-GFP;Twist1*$^{+/-}$ mice six months after suture regeneration and transplanted into one-month-old *Twist1*$^{+/-}$ mice with bilateral coronal suture fusion. For the experiments in Figures 5, 6, 7, S5, and S6G, the suture regeneration surgeries were performed on *Twist1*$^{+/-}$ mice at about two weeks of age after scanning with micro-CT to confirm bilateral coronal suture fusion. For the experiments in Figures S6A–S6F, the suture regeneration surgeries were performed on *Twist1*$^{+/-}$ mice with bilateral coronal suture fusion at about two months of age. For the experiments in Figure S7, two-month-old C57BL/6J mice with defect-producing surgeries at two weeks of age were used as the sham-operated group. Cells from one-month-old C57BL/6J mice were used for 2, 3-D culturing (Figures S2E–S2G) and western blot (Figures S4A and S4B). One-month-old *Gli1-Cre*^{ERT2}*;ROSA26*$^{LoxP\text{-}STOP\text{-}LoxP\text{-}tdTomato}$ *or Gli1-Cre*^{ERT2}*;ROSA26*$^{LoxP\text{-}STOP\text{-}LoxP\text{-}DTA}$ *GFP*

mice were used for cell acquisition and surgery one day post-tamoxifen induction (Figures S3A–S3D). For experiments in Figure S3P, one-month-old *Gli1-Cre^{ERT2};Twist1$^{fl/fl}$* mice were induced with tamoxifen and the coronal suture was collected one month post-induction. Tamoxifen (Sigma, T5648) was suspended in corn oil (Sigma, C8267) at 20 mg/ml and 1.5 mg/10 g body weight was injected intraperitoneally (i.p.) daily for 2 days.

Cell culture, sorting and colony-forming assay

The suture mesenchymal cells were harvested as shown in previous studies (James et al., 2008). Briefly, sagittal and coronal sutures of one-month-old wild-type, *Gli1-Cre^{ERT2};ROSA26$^{LoxP\text{-}STOP\text{-}LoxP\text{-}tdTomato}$* or *Gli1-Cre^{ERT2};ROSA26$^{LoxP\text{-}STOP\text{-}LoxP\text{-}eGFP\text{-}DTA}$* mice were meticulously excised within 0.5 mm of abutting bones on both sides under a dissecting microscope (Leica, M60), while great care was taken to exclude tissue from the posterofrontal and lambdoid sutures. The overlying periosteum and underlying dura mater were removed carefully. The suture tissues were then washed with PBS and αMEM with 100 U/ml penicillin and 100 μg/ml streptomycin several times and were minced into tiny pieces and transferred into a T25 dish (Nest, 705001) at 37°C in an atmosphere of 5% carbon dioxide. Our cell culture medium was formulated following an established protocol for mouse MSCs (Liu et al., 2011) and contained αMEM (GIBCO, 2065542) supplemented with 20% FBS (GIBCO, 2100184), 2 mM L-glutamine (Contained in antibiotics), 55 μM 2-mercaptoethanol (GIBCO, 2090354), 100 U/ml penicillin and 100 μg/ml streptomycin (GIBCO, 2019321). After 5-6 days, cells were digested with TrypLE (GIBCO, 1897328) and the tissues were removed by passing through a 70 μm cell strainer (Falcon, 352350), then the cells were incubated for another 3-4 days before use.

P1 cultured suture mesenchymal cells from *Gli1-Cre^{ERT2};ROSA26$^{LoxP\text{-}STOP\text{-}LoxP\text{-}tdTomato}$* mice were dissociated by TrypLE and resuspended in 500-1000 μl medium. Cells were then filtered with a 40 μm cell strainer (Falcon, 352340) to remove the remaining cell mass and sorted for tdTomato$^+$ cells via flow cytometry in a FACS Aria system using FACS Diva software. After sorting, the tdTomato$^+$ cells were centrifuged for colony-forming assay and suture regeneration. After 7 days, the 24-well culture plates (seeded with 2500 tdTomato$^+$ cells/well) were stained overnight with a mixture solution of 0.1% toluidine blue and 2% paraformaldehyde.

METHOD DETAILS

Intracranial pressure measurement

Intracranial pressure was measured in two-month-old wild-type and *Twist1$^{+/-}$* mice with bilateral suture fusion and six months after coronal suture regeneration surgery at two weeks of age or four and a half months after surgery at two months of age. The procedure was performed as described previously (Murtha et al., 2012) with minor modifications. Briefly, mice were anaesthetized with 2% isoflurane and placed in a stereotaxic setup. A hole was drilled into the right parietal bone that was 2 mm lateral and 2 mm posterior from the Bregma. A 10 μL pipette tip (cut to 5 mm in length) used as the sensor guide was inserted into the hole and fixed with dental cement. After the dental cement dried, the sensor guide was filled with sterile PBS and the fiber-optic intracranial pressure probe (FISO Technologies) was inserted until the tip of the probe touched the dura. Caulking material was applied around the probe and the head of the sensor guide to form an airtight seal. Intracranial pressure was recorded with Evolution software (FISO Technologies).

Behavioral assays

Behavioral characterization of wild-type and *Twist1$^{+/-}$* mice with bilateral suture fusion was carried out at 8-12 weeks of age. As for suture regenerated mice, behavioral assays were performed six months after coronal suture regeneration surgery at two weeks of age or four and a half months after surgery at two months of age; age-matched wild-type and *Twist1$^{+/-}$* mice with bilateral suture fusion were also tested. In all experiments, mice were acclimated to the behavior room at least 60 minutes before the first trial began. Experimenters were blinded to animal genotypes during behavioral tests and data analyses.

Novel object test

This test was performed as described previously (Leger et al., 2013) with minor modifications. Briefly, this test consists of habituation, familiarization, and test phases. In the habituation phase, subject mice were placed in the center of a clean, empty cage and allowed to explore freely for 5 min. After 24 hours, the familiarization phase was performed. Two identical objects were taped to floor along the long axis, 10 cm away from the south and north walls. The mouse was placed in the center of the cage facing the east or west wall and allowed to explore for 10 min. The test phase was performed 3 or 24 hours after the familiarization phase. One of the identical objects was replaced with a novel object with a different shape but similar size. The mouse was placed in the center of the cage facing the east or west wall and allowed to explore for 10 min. The apparatus and objects were thoroughly cleaned with 75% ethanol to remove the olfactory cues between each trial. The entire test phase was videotaped and the travel of the subject mouse was manually documented. The preference index was calculated as $(Tn - Tf)/(Tn + Tf) \times 100\%$, where Tn and Tf represent the time spent exploring novel and familiar objects, respectively.

Three-Chamber Social Interaction Test

The test apparatus was a Plexiglas box containing three compartments connected by small openings that allow the mice free access to each compartment. The subject mouse was first placed in the middle chamber with the side doors closed for 5 min, after which the doors were opened to allow the mouse to explore the three empty chambers. After 10 min of habituation, the mouse was gently guided to the middle chamber and side doors were closed. A stranger mouse was placed in an inverted wire cup in one side chamber and an empty wire cup was placed in the other side chamber. Then the side doors were opened and the subject mouse

was allowed to freely explore the chambers for 10 min. After this period, the subject mouse was again guided to the middle chamber and the doors were closed. A second stranger mouse was placed in the previously empty wire cup. The side doors were opened, and the subject mouse was allowed to freely explore for another 10 min. The amount of time that the subject mouse spent sniffing each wire cup was quantified and the preference index was calculated as (Ts1 − Te)/(Ts1 + Te) × 100% and (Ts2 – Ts1)/(Ts2 + Ts1) × 100%. Here, Te, Ts1 and Ts2 represent the time spent exploring the empty, Stranger 1 and Stranger 2 wire cups, respectively. The apparatus and wire cups were thoroughly cleaned with 75% ethanol to remove the olfactory cues between tests for each mouse.

Rotarod test

The rotarod test consists of training and test phases. Mice were first trained by placing them on a rotating rod (Panlab, Havard Apparatus) at a constant speed of 4 rpm until they were able to stay on the rotating rod for 60 s. The test phase was performed 24 hours after the training phase. The rotarod apparatus was set to accelerate from 4 to 40 rpm in 300 s, and mice were placed on the rod initially rotating at 4 rpm. The latency (time) to falling off the rod was determined. Each mouse was tested three times a day at 15 min intervals for four consecutive days.

Open field

The subject mouse was placed in an empty arena (40 cm × 40 cm) and allowed to freely explore for 15 min. The total traveled distance and time spent in the center zone were recorded and automatically measured using Smart v3.0 (Panlab, Havard Apparatus). The arena was thoroughly cleaned with 75% ethanol between tests for each mouse.

Forelimb grip strength test

This test was performed as described previously (Cabe et al., 1978; Smith et al., 1995). A Grip Strength Meter (Bioseb, BIO-GS3) was used to measure the forelimb grip strength. The gauge was reset and stabilized to 0 g before testing each mouse. A mouse was allowed to grasp the bar mounted on the force gauge and the mouse's tail was slowly pulled back. The peak pull force in grams was recorded on a digital force transducer.

Elevated plus maze test

This test was performed as described previously (Holmes et al., 2002a, 2002b) with minor modifications. Briefly, the elevated plus maze apparatus (Panlab, Havard Apparatus) consisted of two open arms and two closed arms (29.5 × 6 cm). The entire maze was elevated 40 cm from the floor. Mice were individually placed in the center of the maze, facing toward the open arm, and allowed to freely explore the apparatus for 10 min. The open and closed arm entries (all four paws in an arm) and the time spent in the open arms were recorded using Smart v3.0 (Panlab, Havard Apparatus).

Odor discrimination and habituation test

This test was performed as described previously (Arbuckle et al., 2015) with minor modifications. Each mouse was habituated for one hour to a clean new cage before test. Then the animal was presented five odors in a row delivered on cotton swabs in the following order: water, almond flavor, banana flavor, social odor 1 and social odor 2. The almond and banana odors were prepared by diluting almond and citrus extracts (McCormick) in distilled water (1:100). Each social odor was prepared by wiping a cotton swab for 15 s in a zigzag fashion across the bottom of dirty cage which was used to keep mice of the same sex as the test subject. Each odor was presented three times in a row for 2 min each time with approximately 1 min inter-trial interval. For every non-social odor exposure, the cotton swab was freshly prepared by applying 50 μL of diluted odorant. The cumulative time spent sniffing the odor (the animal's nose was oriented toward the cotton tip at a distance less than 2 cm) was manually recorded.

Gel synthesis and testing

Methacrylated gelatin (GelMA) was synthesized as in the previously described (Van Den Bulcke et al., 2000). Briefly, methacrylic anhydride (MA) was added at a rate of 0.4~0.5 ml/min to a 10% gelatin/PBS (w/v) solution at pH 9 under stirring, to achieve a final MA-to-gelatin ratio of 0.3 ml/g. After allowing the reaction to proceed at 50°C for 2.5~3 h, the reacted solution was dialyzed against distilled water at 40°C for 7 days to remove the excessive methacrylic acid and anhydride, then filtered through a 0.22 μm membrane, freeze-dried and stored at −80°C for later use. The substitution degree of GelMA was measured as described previously (Habeeb, 1966), and was found to be approximately 48%. The freeze-dried GelMA was dissolved in αMEM at 5% (w/v) containing 0.5% (w/v) lithium phenyl-2, 4, 6-trimethylbenzoylphosphinate (LAP) to obtain a solution. The GelMA was modified (creating what we refer to here as modified GelMA, or M-GM) by mixing 5% GelMA solution with Matrigel (Corning, 8015323) and 3 mg/mL collagen I (GIBCO, A10483-01) at 4°C with a volume ratio of 10: 2: 1. The M-GM solution was cured with a 365 nm UV light source for few seconds to completely crosslink the hydrogels. Concentration-matched (1) pure GelMA, (2) GelMA:Matrigel at a ratio of 5:1 (creating what we refer to here as GM-Ma), (3) GelMA:Matrigel at 2:1, (4) GelMA: Matrigel at 1:1, (5) GelMA:Matrigel at 1:2, and (6) pure Matrigel were also tested.

Mechanical properties

The mechanical properties of gels were characterized by compression and uniaxial tensile tests using a dynamic mechanical analysis instrument (Instron 5542, Instron, Norwood, MA). For unconfined compression tests, the hydrogels were cured in disks (3 mm thick, diameter as 12 mm) by being exposed to 365 nm UV light (1 W/cm^2) for 2 min. Each sample was placed between two compression plates and compressed at a displacement rate of 1 mm/min. The samples were cut into 2 × 4 × 5 mm^3 strips after photo-cross-linking and stretched at a rate of 1 mm/min to explore the tensile properties. The compression modulus and Young's modulus were calculated as the slope of the linear region in the 0%–10% strain range of the stress-strain curves.

Degradation

The natural degradation properties of the hydrogels were determined in PBS at 37°C for 1, 2, 3, and 4 weeks. At each time point, remaining hydrogel was washed with distilled water, all liquid was removed and gels were lyophilized. The original dry weight was denoted W_o and the dry weight after incubation was W_d. The extent of degradation was determined gravimetrically as the percent weight loss according to following equation: Remaining weight (%) = $(W_o - W_d)/W_d \times 100$.

Diffusion properties

FRAP measurements were performed using confocal laser scanning microscopy (Leica SP8, Germany) to analyze diffusion properties of solutes within the gels as previously reported (Kang et al., 2012; Kaemmerer et al., 2014). Briefly, the gels were loaded with 1 mg/ml FITC-BSA (Invitrogen, A23015). The half time of recovery ($\tau_{1/2}$) and diffusion coefficient were calculated from the experimental recovery curve by fitting of the appropriate FRAP model. All FRAP analyses were performed with MatlabR2019b (Mathworks, Natick, MA, USA). A circular bleach area with a diameter of 50 μm was used throughout all FRAP recordings.

Swelling test

All the gels were photo-cross-linked into a disk shape (thickness = 1 mm, diameter = 12 mm). Then, the gel disks with different compositions were immersed into 2 mL of PBS at 37°C for 24 h to reach equilibrium swelling. After being removed from PBS, the gel disks were gently blotted with a Kimwipe to remove the residual liquid, and the swollen weight of each disk was recorded (W_s). The samples were subsequently lyophilized and weighed again to determine the dry weight of each disk (W_d). The swelling ratio was then calculated as $Q = (W_s - W_d)/W_d$.

Morphology and viability of cells in hydrogels

To characterize the cell morphology in hydrogels, the P1 cultured suture mesenchymal cells were gently mixed with the hydrogel (5×10^5 cells/ml) until uniform and cured with UV light. After 1 or 5 days, samples were fixed with 2.5% glutaraldehyde overnight, washed with PBS three times and fixed with 1% OsO_4 for 1 h. After three more washes, they were dehydrated by a graded series of ethanol (30%, 50%, 70%, 80%, 90%, 95%) for 15 min each and 100% ethanol twice for 20 min each, then transferred to isoamyl acetate twice for 15 min each time. Finally, the samples were carefully moved to a critical point dryer (Leica EM CPD300, Germany) for dehydration. The cross-sections of the samples were exposed and coated with Au/Pd using a sputter coater (Leica EM ACE600, Germany), while the morphology of cells inside the hydrogels was observed using scanning electron microscopy (Nova Nano SEM450, FEI, America).

Cellular viability was detected with a live/dead staining kit (Invitrogen, MP 34958). Briefly, suture mesenchymal cells from sagittal and coronal sutures of one-month-old wild-type mice were mixed with hydrogel at a density of 5×10^5 cells/ml, cured as above, and cultured in αMEM-based medium as described above for 1 or 5 days. Then, the samples were stained with calcein-AM and ethidium homodimer-1 for 30 min. Images were obtained on a Zeiss LSM 710 inverted confocal microscope with a scanning thickness of 3 μm for each layer. The overlaid 2D pictures were analyzed using Leica LAS AF software.

Calvarial defect generation

One-month-old, two-month-old, or two-week-old *Twist1*$^{+/-}$ mice with bilateral coronal suture fusion were chosen for surgery after confirming the fusion via CT scanning. A midline sagittal incision was made on the calvaria under general anesthesia, and the bilateral coronal sutures and the surrounding bones were exposed by elevating the scalp. The overlying periosteum was removed carefully from the exposed area by curette. Then a dental round burr (Brasseler, H52. 11. 003) was used to create a rectangular defect with 0.3-0.4 mm width by referencing the residual hallmark of the fused suture (white arrowheads in Figures 2A, 2C, and 2D) and the landmark for a normal coronal suture (BRG and SQU in Figures S4D–S4F), while carefully avoiding damage to the underlying dura mater. A strip of bone 0.3-0.4 mm wide was preserved between the defect and the sagittal suture. Three types of cells (tdTomato$^+$ cells, heat-inactivated tdTomato$^+$ cells, and cells from *Gli1-Cre*^{ERT2}*;ROSA26*$^{LoxP\text{-}STOP\text{-}LoxP\text{-}eGFP\text{-}DTA}$ mice) were uniformly mixed with M-GM at a density of 5×10^7 cells/ml and 2 μl of the solution was added to the defect. As controls, tdTomato$^+$ cells were mixed with pure GelMA, GM-Ma or Matrigel on ice and then transferred to the defect, or defects were filled with pure M-GM or left empty. All the groups with M-GM were then cured with UV light with a wavelength of 365 nm for a few seconds. The scalp was then sutured closed with 5.0 polyglactin stitches (Figures S3A–S3D).

Suture width

Each calvarial defect was measured six months after surgery to determine the width of the regenerated sutures, and age-matched wild-type mice were used as a control. The distance between the two bones was calculated as the width of the suture, and three points along each suture were selected (the most medial, the most lateral and the middle points of each coronal suture). All measurements were included in the analysis.

Dura mater blocking

After a defect of 0.3-0.4 mm width was generated as above, a Parafilm membrane with 10 nm diameter pores (Thermo Fisher Scientific) was carefully placed between the internal surface of calvaria and the dura mater, while carefully avoiding damage to the dura. Then the defects were filled with M-GM+cells and cured by UV light as outlined above. The calvarial bone together with Parafilm membrane was harvested six weeks later.

Kidney capsule transplantation

We implanted M-GM plus MSCs into the calvarial bone of *Twist1*$^{+/-}$ mice following the removal of the fused coronal suture. One day after this suture regeneration procedure, we removed a 2 mm × 2 mm square area of bone containing M-GM and MSCs. Then we carefully removed the periosteum and dura mater while protecting the M-GM and donor MSCs under a microscope. The explant was then grafted under the kidney capsule of a host mouse as previously described (Xu et al., 2005). The explant was harvested after six weeks.

MicroCT imaging

The calvarial bones and kidney capsules containing calvarial explants were radiographed in live mice using a micro-CT (Ct Lab In-vivo 90) device. Images were collected using a 70 KVp and 114 μA X-ray source. All the 3D reconstructions and sections were analyzed using AVIZO 9.4.0 (Thermo Fisher Scientific).

Immunofluorescence staining and *in situ* hybridization (ISH)

Suture samples were fixed with 4% paraformaldehyde (PFA) in PBS overnight at 4°C, followed by decalcification in EDTA for about 2 weeks, dehydration with a graded sucrose solutions (15% and 30% sucrose for 2 hours each at room temperature, and 30% sucrose with 50% OCT overnight at 4°C) and immediately embedded in OCT (Sakura Finetek, 4583). Frozen tissue blocks were sectioned at 8 μm on a cryostat (Leica) and mounted on SuperFrost Plus slides (Fisher) for staining.

For brain sample sectioning, animals were intracranially perfused with PBS and 4% PFA, and the brain was dissected out, post-fixed with 4% PFA overnight at 4°C, and dehydrated in 30% sucrose solution for 2 days. The dehydrated samples were embedded in OCT and sectioned at 40 μm on a cryostat (Leica).

Sections were permeabilized with blocking buffer containing 1% BSA, 2% goat serum and 0.3% Triton X-100 in PBS for 1 h at room temperature and then incubated with the following primary antibodies: anti-Gli1 (Novus Biological NBP1-78259, 1:20), anti-Runx2 (Cell signaling technology 12556, 1:100), anti-Sp7 (Abcam ab22552, 1:100), anti-FABP4, anti-Collagen II, anti-Osteopontin (R&D systems SC010, 10μg/ml), anti-Cux1 (Santa Cruz Biotechnology SC514008, 1:200), anti-Ctip2 (Abcam ab18465, 1:200), anti-Tbr1 (Abcam ab31940, 1:200), or anti-c-Fos (Cell Signaling Technology 2250, 1:400) overnight at 4°C. The following day, sections were incubated with fluorescently conjugated secondary antibodies: Alexa Fluor 488 goat anti-rabbit IgG (Invitrogen A11008, 1:150), Alexa Fluor 488 donkey anti-goat IgG (Invitrogen A32814, 1:150), Alexa Fluor 488 donkey anti-sheep IgG (Invitrogen A11015, 1:150), Alexa Fluor 647 donkey anti-rabbit IgG (Invitrogen A32795, 1:150) or Alexa Fluor 488 goat anti-chicken IgG (Invitrogen A11039, 1:150) together with DAPI (Thermo Fisher Scientific 62248, 1:1000) for 1 h at room temperature and mounted with Vectashield mounting medium (H-1000, Vector Laboratories). Images were captured by a Leica DMI3000 B fluorescence microscope and a Leica DMI6000 CS confocal microscope using Leica LAS AF software.

To observe the source of Gli1^{+} cells in regenerated sutures, the dura mater right under the coronal suture defect region was labeled very carefully using a Qtracker Cell Labeling kit (Thermo Fisher Scientific, Q25041MP), avoiding surrounding tissues. After staining for 30 min, excess was washed off with PBS, and then the defects were filled with M-GM+MSCs or left empty as mentioned above.

The expression of *Twist1* in the brain and coronal suture of one-month-old wild-type mice was assayed using an RNAscope 2.5 HD Chromogenic Assay (Single-plex, Advanced Cell Diagnostics). Sections were acquired as mentioned above, after which ISH was performed according to the manufacturer's instructions.

Western blot analysis

Suture mesenchymal cells from one-month-old C57BL/6J mice were cultured with 20 μM Wnt agonist 1 (Selleck, S8178) or 100 nM LY2090314 (Selleck, S7063) for one or two weeks in αMEM. Medium was changed every other day. Total protein was extracted using a solution of loading buffer (Cell Signaling Technology, 7723S), protease inhibitor (Thermo Fisher Scientific, 1861278) and DTT (Cell Signaling Technology, 7723S), then separated by 10% SDS-PAGE and transferred to PVDF membranes (Millipore, ISEQ00005). Membranes were blocked with 5% non-fat dry milk dissolved in TBST for 2 hours at room temperature with gentle shaking, and then incubated with primary antibodies: anti-Runx2 (Cell signaling technology 12556, 1:1000), anti-OPN (Abcam ab63856, 1:500), and anti-βactin (Abcam ab20272, 1:1000) at 4°C overnight followed by corresponding horseradish-peroxidase (HRP)-conjugated secondary antibodies. Protein expression was detected by Bio-Rad ChemiDoc Touch (Bio-Rad) and intensities of bands were quantitated by ImageJ software.

RNA sequencing analysis

To determine the differentially expressed genes between seven-month-old C57BL/6J mice (wild-type group, WT), seven-month-old *Twist1*$^{+/-}$ mice (mutant group, MUT), and seven-month-old *Twist1*$^{+/-}$ mice at six months post-surgery (suture regeneration group, REG), RNA sequencing analysis was performed. After removing the periosteum and dura mater, the coronal sutures of WT and REG groups were excised along with less than 0.2 mm of abutting bone on each side under a microscope. A bone sample of the same size was acquired from the coronal suture region of the MUT group. To acquire endogenous cells (tdTomato-negative) from the REG group, 3 mg/ml collagenase type I (Worthington, LS004194) and 4 mg/ml dispaseII (Roche, 04942078001) were used for 1 hour after mincing the regenerated sutures into tiny pieces. Cells were then filtered with a 40 μm cell strainer (Falcon, 352340) to remove the remaining tissue mass and sorted for tdTomato^{-} cells via flow cytometry in a FACS Aria system using FACS Diva software. RNA

was extracted using the RNeasy Micro Kit (QIAGEN, 74004). The quality of RNA samples was determined using an Agilent 2100 Bioanalyzer and all groups had RNA integrity (RIN) numbers > 7.0. cDNA library preparation and sequencing were performed at the University of California, Los Angeles Technology Center for Genomics & Bioinformatics. The paired-end reads with 1 × 75 bp read length were generated on NextSeq500 High Output equipment for three pairs from each group. Raw reads were trimmed, aligned using Partek Flow with the mm10 genome, and normalized using RPKM. Differential expression was estimated by selecting transcripts with a significance of $p < 0.05$. A two-way hierarchical clustering heatmap using Euclidean distance and average linkage was used to display differentially expressed genes from the three groups.

Confirmation of suture MSC stemness

To assay the multipotential differentiation of the regenerated suture cells, cells from *Twist1*$^{+/-}$mice were acquired six months after surgery and cultured following the method described for suture MSCs above. After amplification to sufficient density, the cells were seeded into a 24-well culture plate (Corning, CLS3527) or 15 mL conical tube (Thermo fisher, 362695) and analyzed using a functional identification kit for mouse mesenchymal stem cells (R&D systems, SC010) following the manufacturer's instructions. Osteogenic, adipogenic, and chondrogenic differentiation were performed according to the manufacturer's protocol.

Calvarial injury model

A calvarial injury model was established by creating two circular lesions in the parietal bone using a micro-drill; the periosteum was not removed. The lesions were created bilaterally with a size of ~0.8 mm diameter, 1 mm away from the middle of the coronal suture. The left side was left empty to serve as a control while the right side was filled with M-GM plus donor cells six months after the first suture regeneration surgery. Samples were acquired after three months.

Suture transplantation

The suture transplantation surgery was performed as described in our previous work (Zhao et al., 2015). Six months after suture regeneration in *CAG-EGFP;Twist1*$^{+/-}$ mice with bilateral coronal suture fusion, donor mice were euthanized and a 2 mm × 2 mm square area of bone containing regenerated suture (or for the control group, an equivalent sample of the coronal suture region) was immediately removed under a microscope and kept on ice for later use. The periosteum and dura mater were carefully preserved. One-month-old *Twist1*$^{+/-}$ mice with bilateral coronal suture fusion were used as the recipient mice. A midline sagittal incision was made over the calvaria under anesthesia, and the coronal suture region and surrounding bones were exposed by elevating the scalp. The periosteum in the fused suture area was carefully removed and a 2.2-2.5 mm defect was made in the fused coronal suture region of both sides using a dental round burr (Brasseler, H52. 11. 003) without damaging the underlying dura mater. The suture transplant was placed over the recipient calvarial defect with the dura side facing inside. The scalp was then sutured closed with 5.0 polyglactin suture. Samples were acquired three months later.

Craniofacial shape analysis

Discriminant function analysis (DFA) was established for 3 groups using MorphoJ 1.07a (Klingenberg, 2011) referencing previous work (Parsons et al., 2014). The groups compared were WT (6.5-month-old C57BL/6J mice), MUT (6.5-month-old *Twist1*$^{+/-}$ mice with bilateral coronal suture fusion), and REG (6.5-month-old *Twist1*$^{+/-}$ mice six months after bilateral suture regeneration). The coordinates of each shape were subjected to Procrustes superimposition to place the landmark configurations into a common space using a standard geometric morphometric approach. Subsets of landmarks were used to individually analyze the differences in shape of two distinct regions of the skull (top of calvarium and lateral portion of calvarium). Principal component analysis was used to identify the variation between different groups in both these distinct regions. The landmark subsets are indicated in Figures 6A–6C, and the analysis included a 1,000-round permutation test for Procrustes distance.

MRI analysis

To determine the global and regional brain volume differences between 6.5-month-old C57BL/6J mice (wild-type group, WT), 6.5-month-old *Twist1*$^{+/-}$ mice (mutant group, MUT), and 6.5-month-old *Twist1*$^{+/-}$ mice at six months post-surgery (suture regeneration group, REG), all mice were anesthetized with 4% isoflurane and intracardially perfused with 30 mL of 0.1 M PBS containing 10 U/ml heparin (Sigma, H3149) and 2 mM ProHance (a Gadolinium contrast agent), followed by 30 mL of 4% paraformaldehyde (PFA) containing 2 mM ProHance. Then the mice were decapitated, and brains with skulls were incubated in 4% PFA + 2 mM ProHance overnight at 4°C then transferred to 0.1 M PBS containing 2 mM ProHance and 0.02% sodium azide for 10 days before MRI scanning (Gompers et al., 2017). Magnetic resonance images were acquired on a MRSolutions 7 Tesla MRI scanner (Guildford, UK). Three-dimensional anatomical Fast Spin Echo (FSE) images were acquired to encompass the whole brain. Imaging parameters were as follows: TEeffective/TR = 26ms/400ms, 4 averages, echo train length = 4, field of view = 16 mm × 16 mm × 25.6 mm, matrix size = 160 × 256 × 256, and flip angle = 90°. Total acquisition time was 280 minutes.

The brain region-of-interest boundaries were manually drawn for each slice using ImageJ and a mouse brain anatomical atlas (Allen Mouse Brain Atlas). The measured areas for the whole brain, cortical mantle, hippocampus, thalamus, corpus callosum, and cerebellum were multiplied by slice thickness to calculate final volumes (mm^3).

For all experiments, the number of replicates is stated in the subsection on Quantification and Statistical Analysis (see below) or in the Results section. For sample-size determination, we performed power calculations, in which a p value less than 0.05 was considered as statistically significant difference. For behavioral analyses, based on our preliminary data we determined that the studies required a sample size of n ≅ 10 per genotype of each sex.

Inclusion and exclusion criteria for mouse behavioral test

Criteria for exclusion of mice were predetermined. A preliminary observation of general health and home cage behaviors was conducted for each mouse. Preliminary inspections were used to exclude grossly abnormal mice including mice that lie immobile, do not react to action challenges, do not look to be thriving, or are severely ill. In the rotarod test, mice that could not maintain on the rotarod after the training session or jumped and escaped from the rod or testing bench area were excluded from the analysis. In the novel object test, mice that had less than 15 s of the total sniffing time for both the familiar and novel object were removed from the analysis. In elevated plus maze, mice that made less than three entries into both open and closed arms or fell off of the maze were removed from the analysis. In the open field, three-chamber and odor discrimination/habituation tests, mice that did not engage in the tested behaviors throughout the entire period of behavioral testing were excluded from the analysis.

QUANTIFICATION AND STATISTICAL ANALYSIS

Statistics and reproducibility

SPSS software version 26.0 was used for statistical analysis. Significance was assessed by using independent two-tailed Student's t tests or analysis of variance (ANOVA). *P value*s equal to or lower than 0.05 were considered statistically significant. All of the statistical details of the experiments can be found in the figure legends. Figures S2A–S2D, S2M–S2P, S4A, and S4B show three replicates with independent gels/cells. The experiments in Figures 4E and S2E–S2G were repeated five times with independent cells. Figures S3K–S3N show representative data from over 200 *Twist1*$^{+/-}$ mice. Figures 2G–2R and S3E–S3G show representative data from 10-15 independent experiments. Figures 3A–3H, 4F–4S, S1A, S2H–S2L (three points for each sample), S3H–S3J, S3O, and S3P, show representative data from 5 independent experiments. Each experiment (WT, REG, MUT) in Figures 4A–4D and S4C was repeated three times with sutures/endogenous cells from regenerated sutures/bones from five mice per group. The numbers of mice used in Figures 1, 5, 6, 7, S1B–S1I, and S5–S7 are shown in the figure legends. No methods were used to determine whether the data met assumptions of the statistical approach.

Supplemental Figures

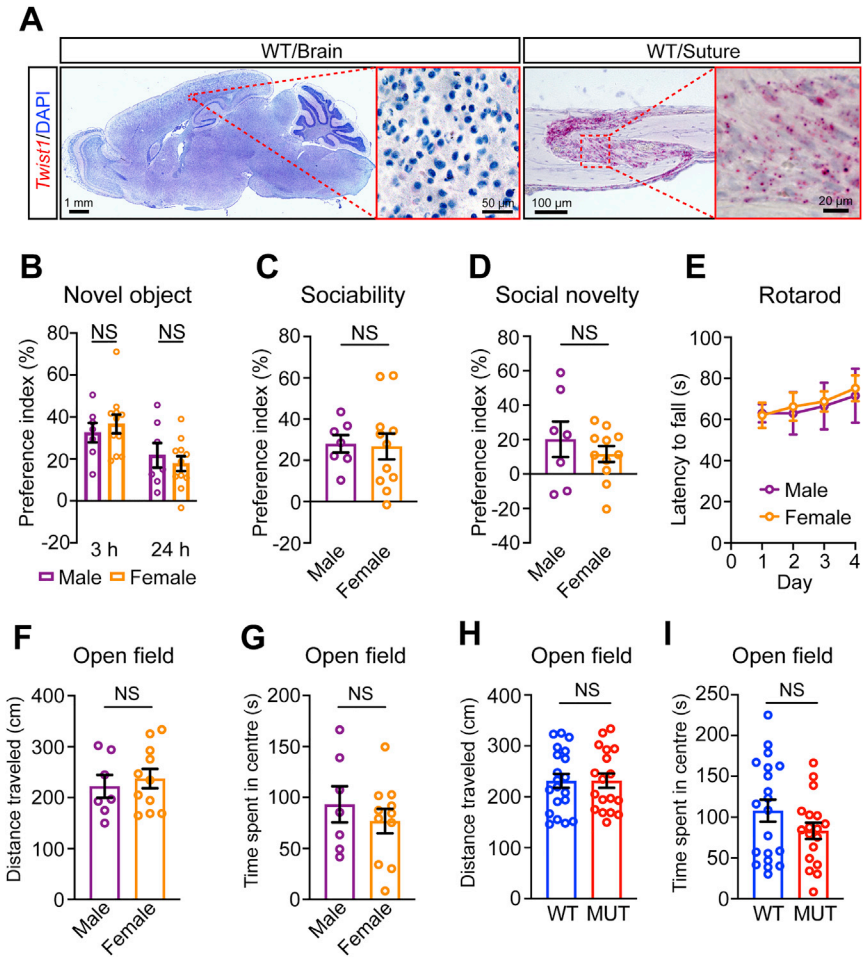

Figure S1. Analyses of *Twist1* Expression and Cognitive and Motor Learning-Related Behavior in Adult Mice, Related to Figure 1

Twist1 is expressed in the cranial suture mesenchyme but is absent from the brain in adult mice. Cognitive- and motor learning-related behavioral deficits of *Twist1*$^{+/-}$ mice are not sex-biased.

(A) *In situ* hybridization of *Twist1* gene transcripts of WT brain (left) and coronal suture (right) of one-month-old C57BL/6J mice. Red signal indicates positive *Twist1* expression.

(B-D) Preference indices for novel object (B), sociability (C) and social novelty (D) during the three-chamber test.

(E) Rotarod performance scored as time on the rotarod.

(F, G) Total traveled distance (F) and time spent in the center area (G) during the open field test (Male, n = 7; Female, n = 11 mice).

(H, I) Total traveled distance (H) and time spent in the center area (I) during the open field test (WT, n = 20; Mut, n = 20 mice).

Data are mean ± s.e.m. (A-J).*p < 0.05, ****p < 0.0001, NS, not significant calculated by two-tailed unpaired t test.

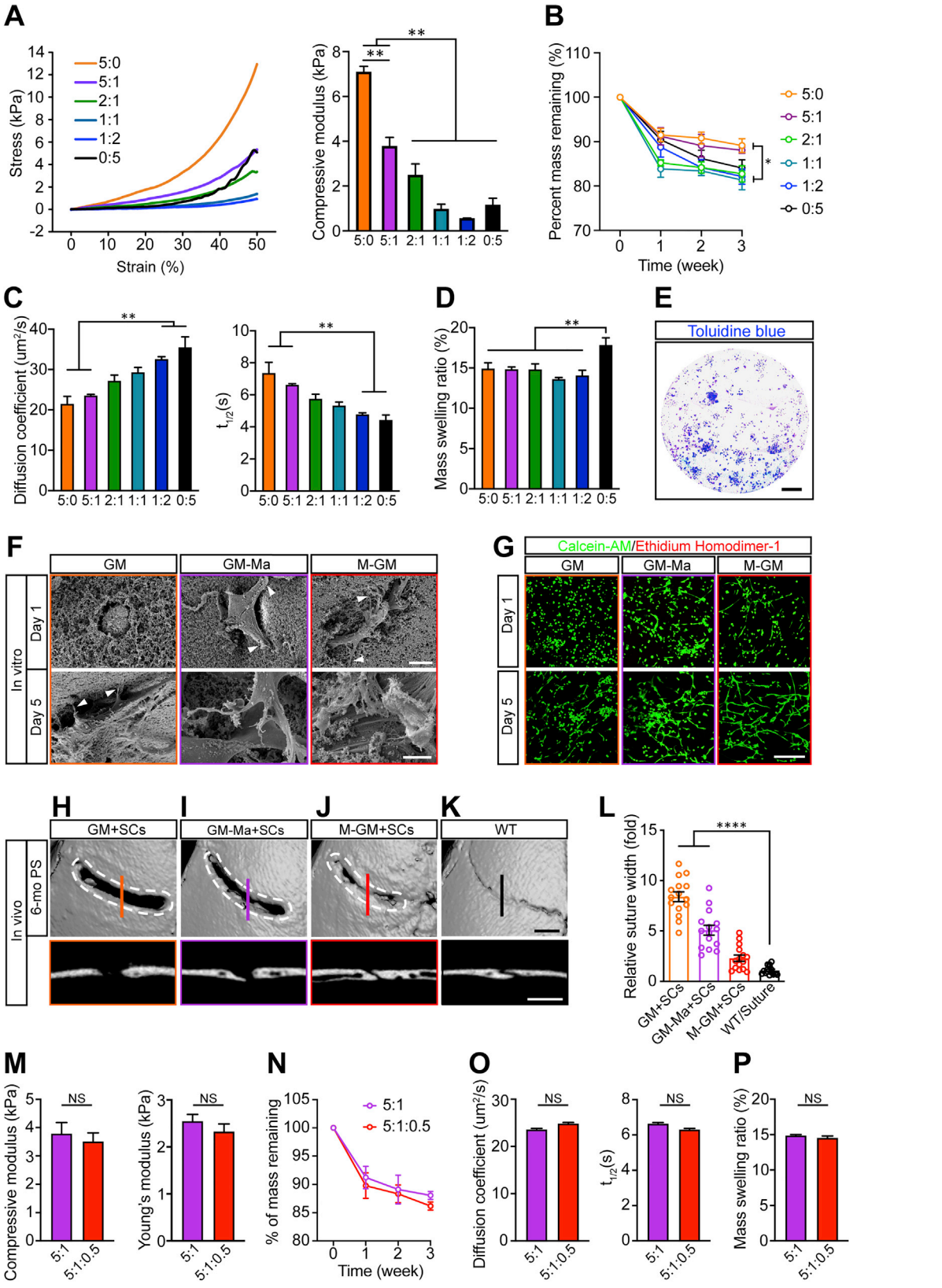

(legend on next page)

Figure S2. GelMA:Matrigel:COL-I at a Ratio of 10:2:1 (M-GM) Provides a Suitable Material for Suture Regeneration, Related to STAR Methods

(A-D) Material properties of (1) pure GelMA (5:0), (2) GelMA:Matrigel at a ratio of 5:1, (3) GelMA:Matrigel at 2:1, (4) GelMA:Matrigel at 1:1, (5) GelMA:Matrigel at 1:2, and (6) pure Matrigel, including compressive modulus (A), degradation rate (B), diffusional permeability (C), and mass swelling ratio (D). Data are expressed as mean ± s.e.m.,*$p < 0.05$, **$p < 0.01$, not significant calculated by one-way ANOVA with Tukey post hoc test.

(E) Toluidine blue staining for colony-forming assay of $Gli1^+$ cells cultured 7 days *in vitro*. Scale bar, 2 mm.

(F) Morphology of cells in pure GelMA (GM) (left), GelMA:Matrigelas 5:1 (GM-Ma) (middle), and M-GM (right) assessed by SEM 1 and 5 days after culturing. Arrowheads indicate pseudopodia. Scale bar, 10 μm in upper panel; 5 μm in lower panel.

(G) Cellular viability detected with live/dead staining kit after 3-D culturing for 1 and 5 days in GM (left), GM-Ma (middle), and M-GM (right). Immunocytochemistry with Calcein-AM (green) for living cells, Ethidium Homodimer-1 (red) for dead cells. Scale bar, 200 μm.

(H-K) Representative microCT images (upper panel, 3-D reconstruction; lower panel, slice) of GM plus suture MSCs (GM+SCs; H), GM-Ma plus suture MSCs (GM-Ma+SCs; I), M-GM plus suture MSCs (M-GM+SCs; J) at six months post-surgery, and the coronal suture of seven-month-old control (K). Dotted lines (white) outline the original surgical defects. Scale bar, 200 μm.

(L) Quantification of suture width (H-K). Data are expressed as mean ± s.e.m. (L). ****$p < 0.0001$, calculated by one-way ANOVA with Tukey post hoc tests.

(M-P) Comparison of material properties of GM-Ma (5:1) and M-GM (5:1:0.5): compressive modulus/tensile strength (M), degradation rate (N), diffusional permeability (O), and mass swelling ratio (P). Data are expressed as mean ± s.e.m., not significant calculated by two-tailed unpaired t test.

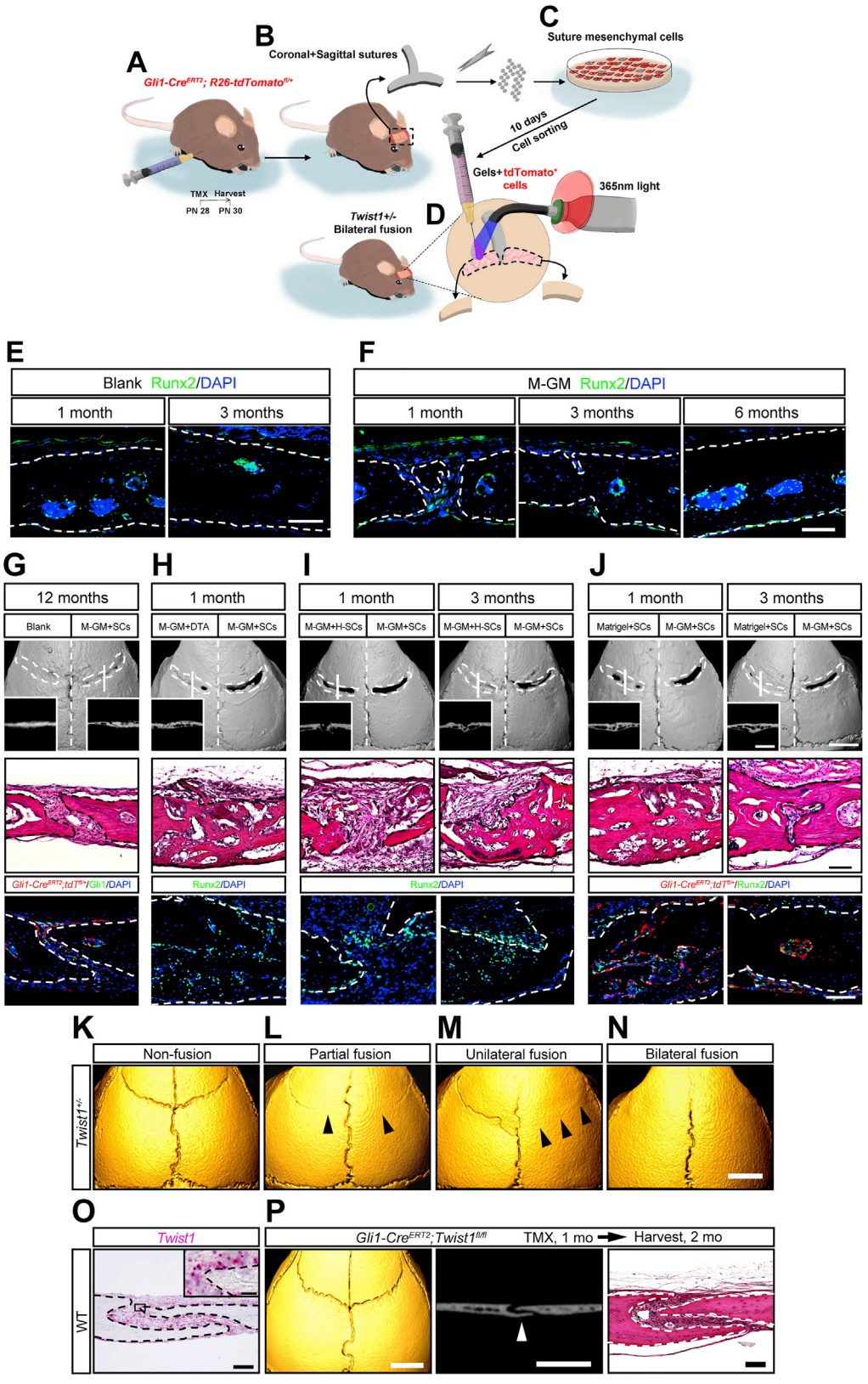

(legend on next page)

Figure S3. Schematic of Suture Regeneration, Related to Figure 2

Gli1^{+} cells and M-GM are required for long-term suture patency. *Twist1*$^{+/-}$ mice show coronal suture fusion with variations. Twist1 in coronal suture of adult mice.

Schematic of suture regeneration surgery

(A) One-month-old *Gli1-Cre*^{ERT2}*;ROSA26*$^{LoxP\text{-}STOP\text{-}LoxP\text{-}tdTomato}$ mice after two days of injection with tamoxifen.

(B) Coronal and sagittal sutures were excised from the mice and minced into tiny pieces for cell culture.

(C) After 10 days of expansion *in vitro*, tdTomato^{+} cells were acquired from suture mesenchymal cells by cell sorting.

(D) After generating defects in the region of the fused sutures, cells mixed with carrier gel biomaterial was placed in the defects and gel was cured with UV light. The wound was then closed carefully.

Implantation of Gli1^{+} cells and M-GM can maintain long-term suture patency

(E, F) Immunofluorescence staining for blank (A, one and three months post-surgery), and M-GM (F, one, three and six months post-surgery) groups. Scale bar, 100 μm.

(G-J) MicroCT imaging (upper panel), HE (middle panel) and immunofluorescence (lower panel) staining of M-GM+SCs one year post-surgery (G), M-GM plus suture mesenchymal cells from one-month-old *Gli1-Cre*^{ERT2}*;ROSA26*$^{LoxP\text{-}STOP\text{-}LoxP\text{-}eGFP\text{-}DTA}$ mice one month post-surgery (M-GM+DTA cells; 1M PS) (H), M-GM plus heat-activated suture MSCs at one month (M-GM+H-SCs; 1M PS) or three months (M-GM+H-SCs; 3M PS) post-surgery (I), matrigel plus Gli1^{+} MSCs at one month (MG+SCs; 1M PS) or three months (MG+SCs; 3M PS) post-surgery (J).

Red fluorescently labeled cells were from one-month-old donor *Gli1-Cre*^{ERT2}*;tdT*$^{fl/+}$ mice (G, J). Insets show CT slices of different regions. Dotted lines in 3-D reconstructed images outline the initial defects. All other white dotted lines represent boundaries of bones.

Scale bars, 1 mm in insets in (G-J); 2 mm in upper panel of (G-J); 100 μm elsewhere.

Twist1$^{+/-}$ mice show coronal suture fusion with variations

(K-N) 3-D reconstructed microCT images of calvaria of one-month-old *Twist1*$^{+/-}$ mice with different coronal suture phenotypes: non-fusion (K), partial fusion (L), unilateral fusion (M), and bilateral fusion (N); arrows in (L, M) point to fused sutures. Scale bar, 2 mm.

Twist1 is not required to support suture patency in adult mice

(O) RNAscope of *Twist1* (red) in the coronal suture of one-month-old wild-type mouse. Scale bar, 100 μm.

(P) 3-D reconstruction (left), microCT slice images (middle), and HE staining (right) of two-month-old *Gli1-Cre*^{ERT2}*;Twist1*$^{fl/fl}$ mice after three days of tamoxifen injection at one month. The arrowhead indicates the coronal suture. White dotted lines indicate boundaries of bones. Scale bars, 2 mm in left, 1 mm in middle and 100 μm in right panel.

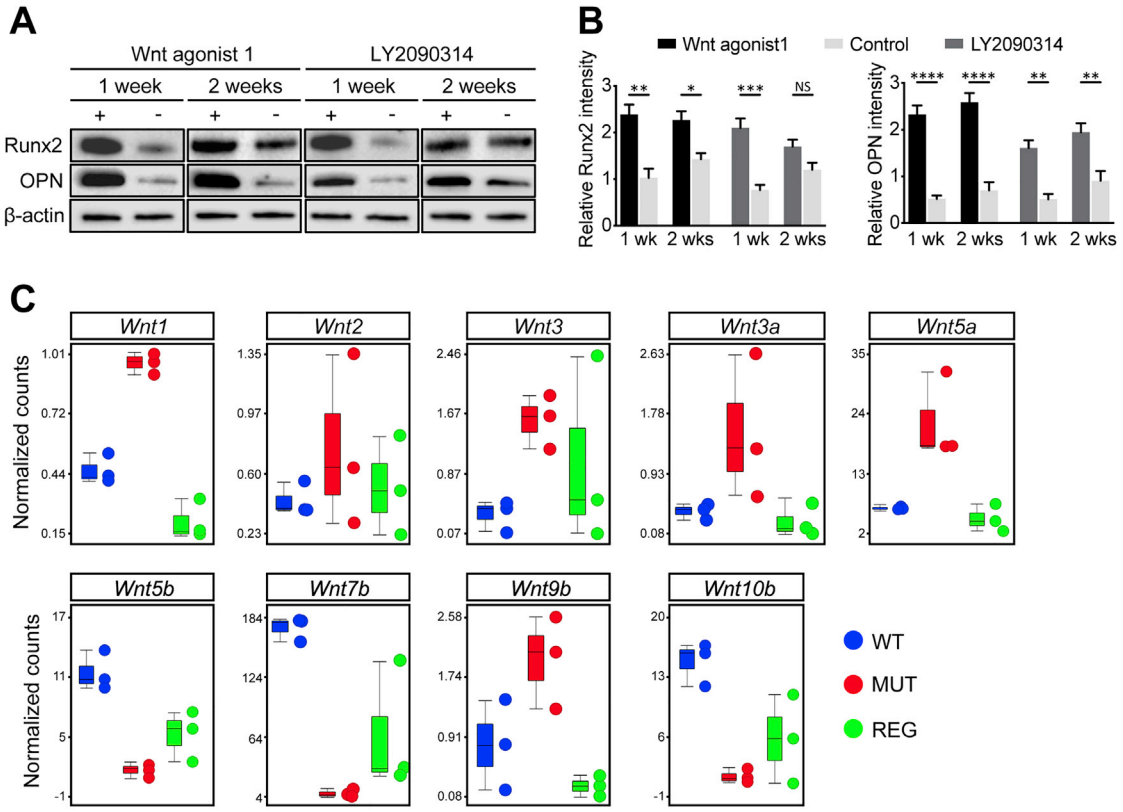

D

Abbreviation	Region	Description
NAS	TC/LC	Nasion; intersection of nasal bones, caudal point
BRG	TC/LC	Bregma; midline intersection of frontal and parietal
PARI	TC/LC	Intersection of parietal bones with anterior aspect of interparietal bone at the midline
OPI	TC/LC	Opisthion; midsagital point on posterior margin of foramen magnum
FSQ	TC/LC	Frontal-squamosal intersection at temporal crest
SQU	TC/LC	Most superior point on the squamous temporal
SQZY	TC/LC	Posterior point at the joining of squamosal body to zygomatic process of squamosal
PIP	TC/LC	Most postero-inferior point on parietal with junction of occipital
PARO	LC	Intersection of interparietal bone with squamous occipital, at the midline

Region: TC = top calvarium; and LC = lateral calvarium.

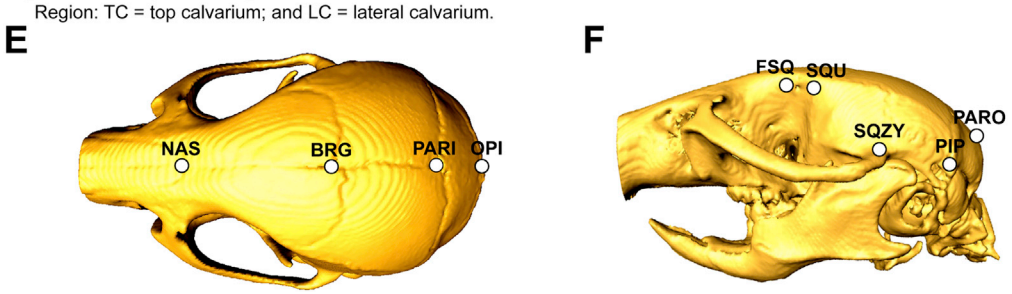

Figure S4. Wnt Signaling Analysis in Craniosynostosis and Suture Regeneration and Landmarks for Analyzing Head Shape, Related to Figures 4 and 5

Wnt signaling is upregulated in craniosynostosis and regenerating suture restores the normal expression of Wnt-related genes

(A) western blot analyses of Runx2 and OPN expression in suture mesenchymal cells after Wnt activator (Wnt agonist 1) or GSK3 inhibitor (activator of Wnt signaling, LY2090314) treatment for one or two weeks.

(B) Quantification of Runx2 and OPN expression after Wnt agonist 1/LY2090314 or vehicle treatment. Data are expressed as mean ± s.e.m., *$p < 0.05$, **$p < 0.01$, ***$p < 0.001$, ****$p < 0.0001$, not significant calculated by two-tailed unpaired t test.

(legend continued on next page)

(C) Signatures of Wnt-related genes based on the relative expression levels of WT, MUT, and endogenous cells from REG.
Landmarks for analyzing head shape
(D) Table of landmark descriptions for analyzing head shape.
(E, F) Superior (E) and lateral views (F) of landmark locations.

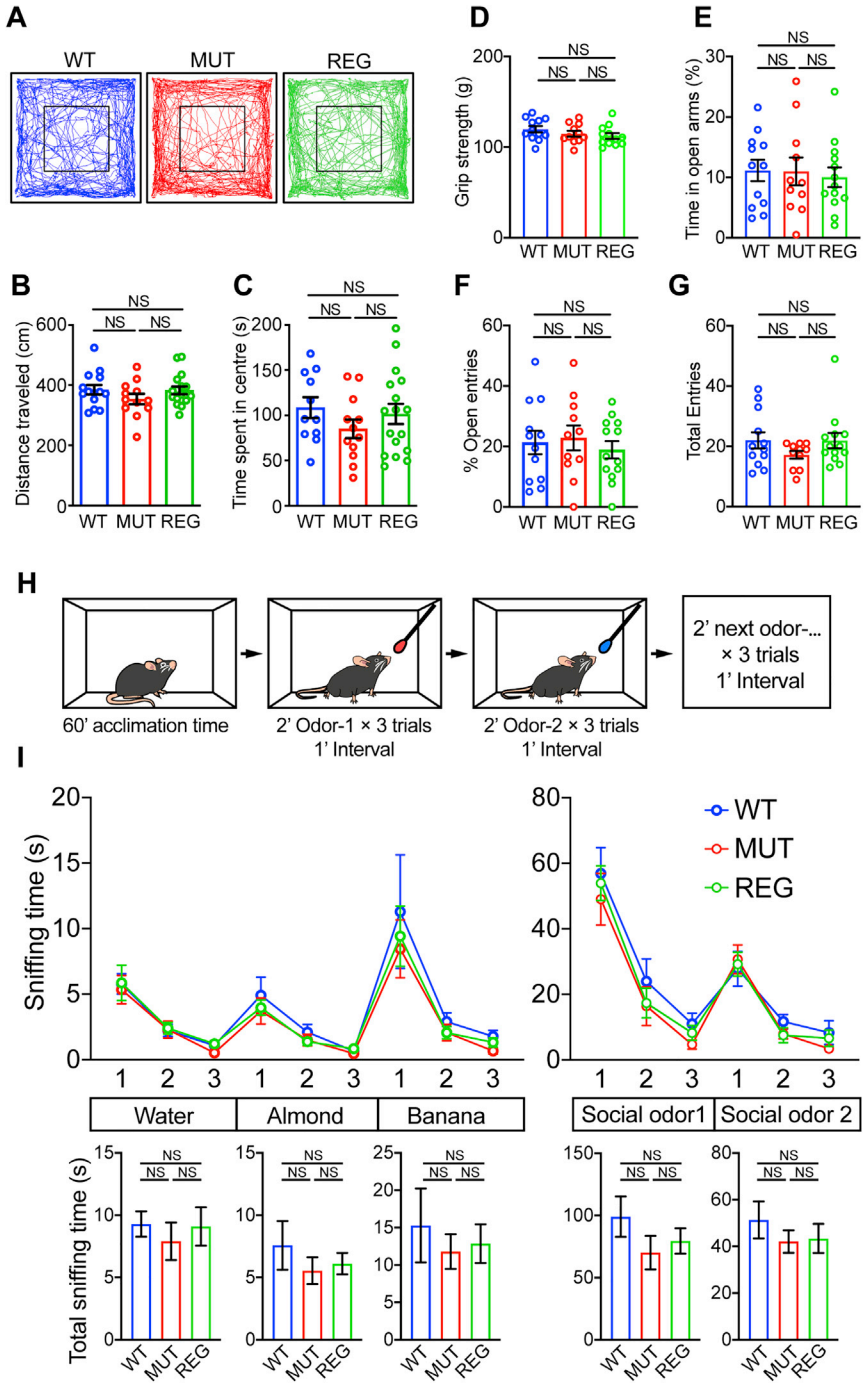

Figure S5. Analyses of Locomotion, Grip Strength, Olfactory Function, and Anxiety-Related Behaviors, Related to Figure 6

(A) Representative tracks of the open field test.

(B, C) Total traveled distance (B) and time spent in the center area (C) during the open field test (WT, n = 11; MUT, n = 12; REG, n = 17 mice).

(D) Comparison of grip strength (WT, n = 12; MUT, n = 11; REG, n = 13 mice).

(E-G) Rate of time spent in open arms (E), number of open entries (F) and total entries (G) during elevated plus maze test (WT, n = 12; MUT, n = 11; REG, n = 13 mice).

(H) Schematic of odor discrimination/habituation test.

(I) Time spent sniffing non-social odors (upper left panel) and social odors (upper right panel) during odor discrimination and habituation test. The lower panel shows the total sniffing time per olfactory cue (WT, n = 12; MUT, n = 11; REG, n = 13 mice).

Data are mean ± s.e.m. (B, C, D, E, F, G, I). **p < 0.01, ***p < 0.001, ****p < 0.0001, NS, not significant calculated by one-way ANOVA with Tukey's test.

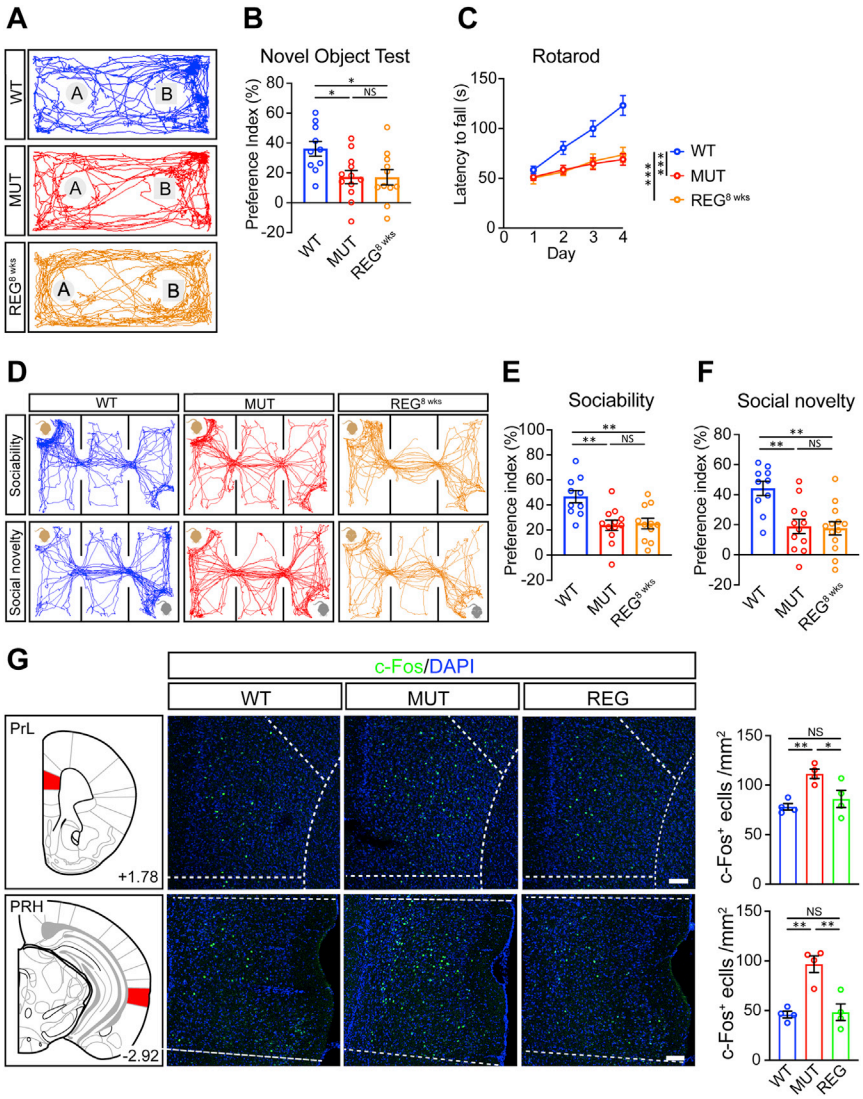

Figure S6. Rescue of Cognitive and Motor Learning Defects of *Twist1*$^{+/-}$ Mice with Craniosynostosis Is Age Dependent (c-Fos Expression Analysis), Related to Figures 6 and 7

Suture regeneration surgery performed at two months of age fails to rescue cognitive and motor learning defects of *Twist1*$^{+/-}$ mice with craniosynostosis

(A, D) Representative animal tracks in novel object test (A) and three chamber test (D).

(B, E, F) Preferential indices in novel object test (B), sociability (E) and social novelty (F) in three-chamber test.

(C) Rotarod performance scored as time (seconds) on the rotarod.

WT, wild-type mice, n = 10; MUT, *Twist1*$^{+/-}$ mice with bilateral suture fusion, n = 12; REG$^{8\ wks}$, *Twist1*$^{+/-}$ mice with suture regeneration surgery performed at two months of age, n = 13. Data are mean ± s.e.m. (B, C, E, F). *p < 0.05, **p < 0.01, ***p < 0.001, ****p < 0.0001, NS, not significant calculated by one-way ANOVA (B, E, F) with Tukey post hoc tests and two-tailed unpaired t test (C).

c-Fos expression analysis

(G) c-Fos is activated at an increased level in the prelimbic and perirhinal cortex in *Twist1*$^{+/-}$ mice, and could be reduced by suture regeneration.

Left panel, schematics of brain coronal sections. Prelimbic cortex (PrL), and perirhinal cortex (PRH) are highlighted with red. The number on the right bottom corner of each panel indicates the distance (mm) from bregma.

Middle panel, representative images of c-Fos expression in PrL (top panel) and PRH (bottom panel). Dotted lines indicate the boundaries of PrL, and PRH. Scale bar, 50 μm.

Right panel, quantification of c-Fos expression in PrL (top panel), and PRH (bottom panel) (WT, n = 4; MUT, n = 4; REG, n = 4 mice). *p < 0.05, **p < 0.01, ***p < 0.001, NS, not significant calculated by one-way ANOVA with Tukey's post hoc test.

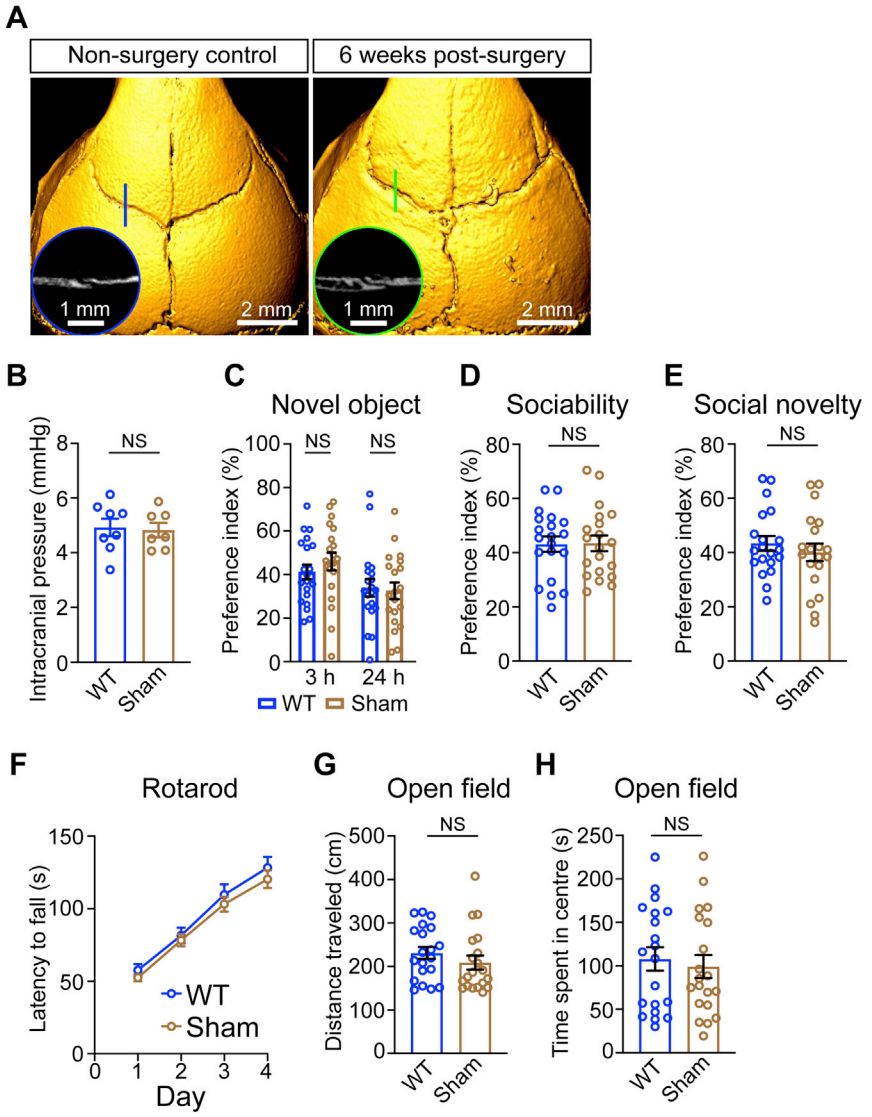

Figure S7. Calvarial Injury Surgery Does Not Cause Elevated ICP or Behavioral Abnormalities, Related to Figure 6

(A) MicroCT images (3-D reconstruction and slice) for wild-type mice at two-weeks-old age before or six weeks post-surgery. Scale bars, 1 mm in inset; 2 mm in (A).

(B) Quantification of ICP values (WT, n = 8; Sham, n = 7 mice).

(C-E) Preference indices of novel object test (C), sociability (D) and social novelty (E) during the three-chamber test.

(F) Rotarod performance scored as time (seconds) on the rotarod (WT, n = 20; Sham, n = 18 mice).

(G, H) Total traveled distance (G) and time (seconds) spent in the center area (H) during the open field test (WT, n = 20; Sham, n = 20 mice).

Data are mean ± s.e.m. (B-H). NS, not significant calculated by two-tailed unpaired t test.